Title: Microtubule networks in zebrafish hair cells facilitate presynapse transport and fusion during development

Saman Hussain[1], Katherine Pinter[1], Mara Uhl[2,3], Hiu-Tung Wong[1], and Katie S. Kindt[1]

[1]Section on Sensory Cell Development and Function, National Institute on Deafness and other Communication Disorders, Bethesda, MD, 20892, USA

[2]Presynaptogenesis and Intracellular Transport in Hair Cells Junior Research Group, Institute for Auditory Neuroscience and InnerEarLab, University Medical Center Goettingen, 37075 Goettingen, Germany

[3]Collaborative Research Center 889 '*Cellular Mechanisms of Sensory Processing*', 37075 Goettingen, Germany

Correspondence: katie.kindt@nih.gov

Abstract

Sensory cells in the retina and inner ear rely on specialized ribbon synapses for neurotransmission. Disruption of these synapses is linked to visual and auditory dysfunction, but it is unclear how these unique synapses form. Ribbon synapses are defined by a presynaptic density called a ribbon. Using live imaging in zebrafish hair cells, we find that numerous small ribbon precursors are present throughout the cell early in development. As development progresses, fewer large ribbons remain, and localize at the presynaptic active zone (AZ). Using tracking analyses, we show that ribbon precursors exhibit directed motion along an organized microtubule network to reach the presynaptic AZ. In addition, we show that ribbon precursors can fuse together on microtubules. Using pharmacology, we find that microtubule disruption interferes with ribbon motion, fusion, and normal synapse formation. Overall, this work demonstrates a dynamic series of events that underlies the formation of a critical synapse required for sensory function.

Introduction

The inner ear and retina contain sensory cells with specialized ribbon synapses that faithfully transmit the timing, duration, and intensity of sensory stimuli to the brain. These synapses are critical for hearing, balance, and vision, and their disruption is linked to auditory, vestibular, and visual disorders (Frederick and Zenisek, 2023; Kujawa and Liberman, 2015; Wan et al., 2019). The hallmark feature of these synapses is the presynaptic ribbon, a dense body made up primarily of the protein Ribeye (Schmitz et al., 2000). Ribbons are found at the presynaptic active zone (AZ) and act as scaffolds to ready synaptic vesicles for release (Schmitz, 2009). Work in fixed tissues has led to the hypothesis that small ribbon precursors migrate to the AZ and fuse to form larger, mature ribbons. However, direct evidence for these dynamic processes during ribbon formation has not yet been demonstrated.

Neurotransmission at mature ribbon synapses is triggered in response to graded membrane depolarizations dictated by the duration and intensity of sensory stimuli. Membrane depolarization opens voltage-gated calcium channels (Ca_V1) beneath ribbons (Brandt et al., 2003; Chang et al., 2006) (see schematic in Figure 1C). Calcium influx triggers synaptic vesicle fusion and the release of glutamate onto postsynaptic receptors (Obholzer et al., 2008; Ruel et al., 2008). Studies have shown Ribeye, the core component of the ribbon, is essential for the formation and function of ribbon synapses in both mouse and zebrafish (Becker et al., 2018; Jean et al., 2018; Lv et al., 2016; Maxeiner et al., 2016). Other key components include the classic neuronal scaffolding proteins Bassoon and a novel variant of Piccolo, Piccolino (Gundelfinger et al., 2016). In mice, the loss of Bassoon disrupts ribbons anchoring and synapse function (Dick et al., 2003; Frank et al., 2010; Khimich et al., 2005). In rats, the loss of Piccolino also impacts ribbon morphology (Michanski et al., 2023; Regus-Leidig et al., 2014). Currently how these key molecular players fit within the dynamics underlying ribbon formation is unclear.

In neurons, precursor vesicles containing Piccolo and Bassoon are transported along microtubules to the developing presynaptic AZ. (Ahmari et al., 2000; Gundelfinger et al., 2016; Maas et al., 2012; Shapira et al., 2003). This transport requires molecular motors, along with adaptor proteins (Bury and Sabo, 2011; Fejtova et al., 2009; Maas et al., 2012). In neurons, kinesins are the molecular motors that transport cargo in the anterograde direction–towards

60 the presynaptic AZ–while cytoplasmic dynein mediates retrograde transport, back to the cell
61 soma (Sweeney and Holzbaur, 2018). Although the kinesin responsible for Piccolo-Bassoon
62 vesicle transport is not known, recent work in *Drosophila* and *C. elegans* suggests that the
63 kinesin KIF1A may transport AZ components (Oliver et al., 2022; Pack-Chung et al., 2007). Work
64 in developing photoreceptors and mouse auditory inner hair cells (IHCs), has shown that ribbon
65 precursors contain not only Ribeye, but also Bassoon, and Piccolino (Regus-Leidig et al., 2009;
66 Michanski et al., 2019). Whether ribbon precursors are actively transported along microtubules
67 during synapse formation is not known.

68 The formation of ribbon synapses has been extensively studied using light and electron
69 microscopy in fixed tissues (Michanski et al., 2019; Regus-Leidig et al., 2009; Schmitz, 2009;
70 Sheets et al., 2011; Sobkowicz et al., 1986, 1982). In mouse auditory IHCs, this process occurs
71 over an extended time period (E18-P14) (Michanski et al., 2019; Sobkowicz et al., 1986, 1982),
72 while in zebrafish hair cells, ribbon synapses mature in just 12-18 hrs (Dow et al., 2015; Sheets
73 et al., 2011). Early development in both mouse IHCs and zebrafish hair cells features many small
74 ribbon precursors throughout the cell, likely formed via Ribeye self-aggregation in the cytosol
75 (Magupalli et al., 2008; Schmitz et al., 2000). As development progresses, ribbons enlarge,
76 localize to the presynaptic AZ, and associate with the innervating afferent terminals. Finally, the
77 number of ribbons associated with postsynaptic machinery is refined to obtain the proper
78 number of complete synapses. Recent work in mice has shown that ribbon precursors associate
79 with microtubules (Michanski et al., 2019), and it has been proposed that ribbon precursors
80 may migrate along microtubules to reach the presynaptic AZ, although the *in vivo* dynamics of
81 this process remain unclear.

82 To study ribbon formation, we examined hair cells and developing ribbons in the
83 zebrafish lateral line (Figure 1A), a sensory system that allows aquatic vertebrates to sense local
84 water movements (Freeman, 1928; Suli et al., 2012). The lateral line consists of clusters of hair
85 cells called neuromasts that are arranged in lines along the surface of the fish. In the posterior
86 lateral line (pLL), which forms an array of neuromasts along the zebrafish trunk, hair cells
87 emerge at 2 days post fertilization (dpf) (see Figure 1A-B,D), and the lateral-line system reaches
88 functional maturity by 5 dpf (Suli et al., 2012). At these larval ages zebrafish are transparent,

89 which enables *in vivo* imaging of ribbon formation over extended periods (Dow et al., 2015).
90 Further, transgenic lines expressing fluorescently tagged proteins allow high-resolution
91 visualization of subcellular dynamics, including ribbon formation.
92 During our study, we worked in close collaboration with another group investigating the
93 late stages of ribbon formation in mouse auditory IHCs (postnatally). This work is published in a
94 companion paper (Voorn et al., 2024). Together our studies demonstrate that ribbon transport
95 along microtubule networks is essential for proper ribbon formation in mice and zebrafish. Our
96 zebrafish work leverages transgenic lines that label: developing ribbons, microtubule networks,
97 and the growing plus ends of microtubules. We use these lines, along with high-resolution
98 imaging to visualize the dynamics of ribbon formation. Using live imaging, we show that early in
99 development, many small ribbon precursors are distributed throughout the cell. By later stages,
100 fewer large ribbons remain and localize to the base of the cell. We show that microtubule
101 networks in lateral-line hair cells are dynamic and grow plus ends towards the presynaptic AZ,
102 the preferred direction for most kinesin motors (Sweeney and Holzbaur, 2018). Tracking
103 analyses reveal the directed motion of ribbon precursors towards the presynaptic AZ, with
104 ribbon precursors moving along and fusing on microtubules. Further, an intact microtubule
105 network is critical for ribbon transport, fusion, and synapse formation. Overall, this
106 foundational work provides insight into ribbon formation and the processes needed to reform
107 ribbon synapses for the treatment of auditory and vestibular synaptopathies.
108

109 **Results**

110 **Time course of ribbon formation in living zebrafish lateral-line hair cells**

111 Fixed preparations in zebrafish and mice have outlined a conserved process that underlies
112 ribbon or presynapse development in hair cells (Michanski et al., 2019; Sheets et al., 2011). To
113 examine the time course underlying ribbon formation *in vivo*, we studied hair cells in the
114 zebrafish pLL. These hair cells form 3-4 ribbon synapses in just 12-18 hrs (Dow et al., 2015;
115 Kindt et al., 2012). To image hair cells, ribbon precursors, and ribbons *in vivo* we used a double
116 transgenic line. One transgenic line labels microtubules and serves as a marker of hair cells
117 (*myo6b:YFP-tubulin*). The other transgenic line reliably labels ribbons and smaller ribbon

118 precursors (*myo6b:riba-TagRFP*) in hair cells (see example: Figure 1D). Although this latter
119 transgene expresses Riba-TagRFP under a non-endogenous promoter, neither the tag nor the
120 promoter ultimately impacts cell numbers, synapse counts, or ribbon size (Figure 1-S1A-E).
121 For our initial analyses, we assessed the overall time course of ribbon formation in hair
122 cells in the posterior lateral line (pLL) when larvae were 2 dpf (Figure 1A). At 2 dpf each pLL
123 neuromast contains 4-8 developing hair cells at different developmental stages (Figure 1B,D,F-
124 I). We staged hair cells based on the development of the apical, mechanosensory hair bundle.
125 The hair bundle is composed of actin-based stereocilia and a tubulin-based kinocilium. We used
126 the height of the kinocilium (see schematic in Figure 1B), the tallest part of the hair bundle, to
127 estimate the developmental stage of hair cells as described previously (stage: hair bundle
128 height; early: < 1.5 µm, intermediate: 1.5-10 µm, late: 10-18 µm, mature: > 18 µm (Zhang and
129 Kindt, 2022)). Qualitatively, we observed that at early and intermediate stages, small Riba-
130 TagRFP puncta were present throughout the cell body (see examples: Figure 1D,F-G). By late
131 stages, or in newly matured hair cells, larger Riba-TagRFP puncta were restricted to the base of
132 the cell (see example: Figure 1H-I). We quantified the total number of Riba-TagRFP puncta
133 based on developmental stage and found that the total number of puncta was high at early and
134 intermediate stages but significantly decreased when hair cells were mature (Figure 1E, Figure
135 1-S2A, n = 7 neuromasts and 67 hair cells).
136 When taking these live images, we had no postsynaptic marker and were unable to
137 differentiate between precursors and smaller ribbons associated with a postsynaptic density.
138 Therefore, we classified all apical Riba-TagRFP puncta above the nucleus as precursors, and all
139 ribbons located beneath the nucleus at the cell base as more mature ribbons. Using this
140 classification, we quantified the total number of Riba-TagRFP puncta at each developmental
141 stage (Figure 1E, Figure 1-S2B-C, n = 7 neuromasts and 67 hair cells). We found that apical Riba-
142 TagRFP precursors were only present at early and intermediate stages (Figure 1E, Figure 1-S2B,
143 and see yellow arrows in Figure 1F-G). In contrast, hair cells at late or mature stages contained
144 more mature ribbons located at the cell base, below the nucleus (Figure 1E,H-I, Figure 1-S2C).
145 Overall, our live images examining Riba-TagRFP puncta show a similar, developmental process

146 as observed in fixed preparations–the number of ribbons and precursors decrease and become
147 basally localized to the presynaptic AZ as the hair cell develops.
148
149 **Microtubules grow plus ends toward the presynaptic active zone in hair cells**
150 An important question in ribbon formation is how ribbons and precursors migrate to the
151 presynaptic AZ. Work on mouse IHCs using electron microscopy (EM) and super-resolution
152 microscopy found that developing ribbons and precursors often associate with microtubules
153 (Michanski et al., 2019). Similar to what was observed in mice using EM, in living, pLL hair cells
154 we observed ribbon precursors associated with microtubules (see yellow arrows in Figure 1F-
155 G). Based on these association studies, a microtubule network may function to transport ribbon
156 precursors during development. To understand if ribbons could be transported along
157 microtubules, we first examined the composition and polarity of the microtubule network in
158 pLL hair cells.
159 We first examined the composition, or posttranslational modifications present in the
160 microtubule network in pLL hair cells using immunohistochemistry. Using this approach, we
161 labeled either acetylated- (modification found in mechanically stabilized microtubules) or
162 tyrosinated- (modification found in destabilized microtubules) α-tubulin (Janke and Magiera,
163 2020). We performed our staining in a transgenic line that labels all microtubules (*myo6b:YFP-*
164 *tubulin*). We found that in pLL hair cells, the microtubule network extends along the apical-
165 basal axis of the cell and is highly acetylated; acetylated microtubules are more concentrated at
166 the cell apex (Figure 2-S1A-C). Outside of the kinocilium, we did not observe tyrosinated
167 microtubules in pLL hair cells. Instead, tyrosinated microtubules were observed in the zebrafish
168 skin, pLL nerve terminals, and the supporting cells that surround hair cells (Figure 2-S1D-F).
169 Overall, our immunostaining results indicate that in pLL hair cells, a considerable portion of the
170 microtubule network is highly acetylated. Acetylation may provide a population of mechanically
171 stable microtubules that could be used to transport ribbon precursors.
172 Although microtubule modifications are informative, these labels do not provide
173 definitive information regarding microtubule growth or polarity. Knowing microtubule polarity
174 is important, as many cargos are transported based on polarity. For example, most kinesin

175 motor proteins transport cargo toward the more dynamic plus end of microtubules (Sweeney
176 and Holzbaur, 2018). Therefore, to explore microtubule polarity in pLL hair cells, we created a
177 transgenic line that expresses the plus-end marker of microtubules, EB3 (end-binding protein
178 3), fused with GFP (see example: Figure 2A, *myo6b:EB3-GFP*). Previous work in other cell types
179 has shown that EB3-GFP can be used to visualize the plus end of growing microtubules (Kawano
180 et al., 2022; Stepanova et al., 2003).

181 We used this transgenic line, along with confocal microscopy to visualize microtubule
182 growth in pLL hair cells (z-stacks every 7 s for 20-30 min). By imaging EB3-GFP dynamics, we
183 observed comet-like tracks that allowed us to visualize the plus end of growing microtubules
184 (see Movie S1). In hair cells, microtubule organizing centers are located beneath a single
185 microtubule-based kinocilium, the primary cilium in hair cells (Lepelletier et al., 2013).
186 Consistent with studies in motile cilia, we observed foci of EB3-GFP at the tips of kinocilia that
187 emanate away from the apex of the cell body (Schrøder et al., 2011) (Figure 2-S2A-C). This
188 result suggests that similar to other cilia, the plus ends of kinocilia are towards their tips, away
189 from the cell body. In addition, we observed EB3-GFP tracks within the soma of hair cells and
190 found that the majority of tracks were directed away from the cell apex and towards the base
191 of the cell (see EB3-GFP images taken from Movie S1, with tracks rendered into a pseudocolor
192 image based on time, Figure 2C-D). To quantify the direction of EB3-GFP tracks we used Imaris
193 to perform 2D analyses to detect and create vectors of EB3-GFP tracks (see arrows; Figure
194 2B,E,F). We aligned these vectors along the 2D apical-basal axis of each cell. Here vector
195 movement towards the apex was represented as 180°, and movement to the base was
196 represented at 0° (see schematic, Figure 2G). The movement of EB3-GFP vectors was quantified
197 as the angle between 0 and 180°. From this analysis, we found that 78 % of EB3-GFP vectors
198 were directed towards the base in pLL hair cells (Figure 2G, 2014/2597 tracks < 90°, n = 7
199 neuromasts and 33 hair cells).

200 Overall, our immunostaining revealed that the soma of hair cells contains a population
201 of microtubules stabilized by acetylation. Our *in vivo* imaging of EB3-GFP revealed that within
202 this population there is extensive microtubule dynamics, and the plus ends of microtubules are
203 primarily directed towards the cell base, and the presynaptic AZ.

204

205 **Ribbon precursors associate with and show directed motion along microtubules**

206 Our analysis of microtubule dynamics using EB3-GFP indicates that the plus ends of
207 microtubules point toward the cell base (Figure 2). Therefore, we hypothesized that these
208 tracks of microtubules could be used by kinesin motor proteins to transport precursors from
209 the cell apex to the base during development. To test this hypothesis, we used either Airyscan
210 or Airyscan 2 confocal imaging to capture timelapses of ribbon and precursor movement for
211 longer durations (Airyscan: ~3 µm z-stacks (15-20 slices) every 50-100 s for 30-70 min) or for
212 shorter total durations with a faster capture rate (Airyscan 2: ~2-3.5 µm z-stacks (12-20 slices)
213 every 3-20 s for 5-40 min). We focused our analysis on developing pLL hair cells at early and
214 intermediate stages when ribbon precursors are abundant throughout the cell (Figure 1D,F-G).
215 For this work we used Riba-TagRFP to mark ribbons and precursors, and YFP-tubulin to label
216 microtubules and provide cellular context.

217 From our timelapses, we observed that similar to our initial live analyses (Figure 1F-G),
218 ribbon precursors associate with microtubules and are not found free-floating and untethered
219 in the cell (Movie S2, S3). We observed that precursors exhibited 3 main movement behaviors
220 related to microtubule association. First, we observed that the majority of precursors
221 associated with microtubules remained stationary or confined (see examples: Figure 3C top two
222 panels, Figure 3D,E asterisks, Movie S4). Second, we also observed rapid movement of
223 precursors–during this movement, precursors appeared to be in close association with
224 microtubules (see examples: Figure 3C bottom 4 panels, Figure 3D,E yellow arrowheads, Figure
225 3-S1A,B, Movie S4, S5, S6). This movement along microtubules occurred bidirectionally,
226 towards the cell apex and towards the base (Figure 3C, middle panels (arrows to base), bottom
227 panels (arrows to apex), Figure 3D-E, Figure 3-S1A and Movie S4, S5 (to base), Figure 3-S1B and
228 Movie S6 (to apex)). Third, during the timelapses, we often observed that precursors switched
229 associations between neighboring microtubules (Figure 3-S1C-D, Movie S7, 2.8 switching events
230 per neuromast, n = 10 neuromasts).

231 To quantify ribbon and precursor movement, we used Imaris to obtain x,y,z coordinates
232 for each ribbon during our timelapses (longer 30-70 min acquisitions) (see examples: Figure 3A-

233 C, Movie S2, S3). This analysis yielded tracks or trajectories for all precursors and ribbons. We
234 then performed a mean-squared displacement (MSD) analysis on ribbon tracks to classify the
235 type of motion we observed. In this analysis, the exponent (α) of MSD vs time is obtained by
236 curve fitting. A value of $\alpha > 1$ indicates directional motion with velocity, $\alpha = 1$ indicates
237 Brownian motion, and $\alpha < 1$ is representative of confined motion or subdiffusion (Figure 3F,G)
238 (Sikora et al., 2017). This method allows us to determine what type of motion each track is
239 exhibiting. Our results show that in developing hair cells, ribbon tracks exhibit directional as
240 well as confined motion (Figure 3H, example MSD tracks with $\alpha > 1$ (red tracks, top panel) and α
241 < 1 (black tracks, bottom panel) from 2 neuromasts). Upon quantification, 20.2 % of ribbon
242 tracks show $\alpha > 1$, indicative of directional motion, but the majority of ribbon tracks (79.8 %)
243 show $\alpha < 1$, indicating confinement on microtubules (Figure 3I, n = 10 neuromasts, 40 hair cells,
244 and 203 tracks).
245 To provide a more comprehensive analysis of precursor movement, we also examined
246 displacement distance (Figure 3J). Here, as an additional measure of directed motion, we
247 calculated the percent of tracks with a cumulative displacement > 1 µm. We found 35.6 % of
248 tracks had a displacement > 1 µm (Figure 3K; n = 10 neuromasts, 40 hair cells, and 203 tracks).
249 Of the tracks with displacement > 1 µm, the majority of ribbon tracks (45.8 %) moved to the cell
250 base, but we also found a subset of ribbon tracks (20.8 %) that moved apically (33.4 % moved in
251 an undetermined direction) (Figure 3L). This apical movement is consistent with a
252 subpopulation of microtubules showing plus-end mediated growth apically (22.8 % of EB3-GFP
253 tracks). In addition, we examined the location of precursors within the cell that exhibited
254 displacements > 1 µm. We found that 38.9 % of these tracks were located above the nucleus,
255 while 61.1 % were located below the nucleus (Figure 3M). Overall, our timelapse imaging
256 demonstrated that ribbons and precursors displayed 3 main types of movement on
257 microtubules: confinement, movement along microtubules, and switching between
258 microtubules. Further, our tracking analyses indicate that while the majority of precursors are
259 confined on microtubules, a subpopulation of ribbons and precursors exhibit directional
260 motion.
261

262 **Long-term manipulation of microtubules impacts ribbon formation**

263 Our timelapse imaging revealed that precursors and ribbons can move along directionally
264 microtubules. To assess the importance of the microtubule network in synapse formation we
265 used pharmacology to destabilize or stabilize the microtubule network in pLL hair cells using
266 nocodazole or taxol respectively. We incubated larvae at 2 dpf for 16 hrs (56-72 hours post
267 fertilization (hpf)), a time window that encompasses a large portion of synapse formation in
268 developing hair cells. After these pharmacological treatments, we fixed and immunostained
269 larvae to label acetylated-α-tubulin, to monitor changes to the microtubule network. In
270 addition, we co-labeled with Ribeyeb to label ribbons and precursors and pan-Maguk to label
271 postsynapses.

272 After a 16-hr treatment with 250 nM nocodazole, we observed a decrease in acetylated-
273 α-tubulin label (qualitative examples: Figure 4A,C, Figure 4-S1A-B). Quantification revealed
274 significantly less mean acetylated-α-tubulin label in hair cells after nocodazole treatment
275 (Figure 4-S1D). Less acetylated-α-tubulin label indicates that our nocodazole treatment
276 successfully destabilized microtubules. We also examined the number of hair cells per
277 neuromast and observed that after nocodazole treatment, there were significantly fewer hair
278 cells compared to controls. This indicates that either nocodazole is slightly toxic or interferes
279 with cell division. Both situations have been observed previously during nocodazole treatments
280 in other systems (Gupta, 1985; Zieve et al., 1980). We next examined the Ribeyeb label in hair
281 cells to assess precursors and ribbons. We found that after nocodazole treatment, the total
282 number of Ribeyeb puncta (apical and basal) per hair cell was significantly higher compared to
283 controls (Figure 4G). We also observed that the average of individual Ribeyeb puncta (from 2D
284 max-projected images) was significantly reduced compared to controls (Figure 4H). Further, the
285 relative frequency of individual Ribeyeb puncta with smaller areas was higher in nocodazole-
286 treated hair cells compared to controls (Figure 4I). We also examined the number of complete
287 synapses (Ribeyeb-Maguk paired puncta) per hair cell after nocodazole treatment. We found
288 that there were significantly fewer complete synapses per hair cell after a 16-hr nocodazole
289 treatment (Figure 4F). Our long-term nocodazole treatment indicates that microtubule

290 destabilization led to an increase in ribbons and precursors while reducing the number of
291 synapses per cell.
292 We performed a similar analysis on hair cells after a 16-hr treatment with 25 µM taxol.
293 After treatment we observed more acetylated-α-tubulin label, indicating that our taxol
294 treatment successfully stabilized microtubules (qualitative examples: Figure 4-S1A,C, Figure 4-
295 S2A,C). Quantification revealed an overall increase in mean acetylated-α-tubulin label in hair
296 cells after taxol treatment, but this increase did not reach significance (Figure 4-S1E). Unlike
297 nocodazole treatment, taxol did not significantly impact the number of hair cells, the average
298 area of Ribeyeb puncta, or the number of ribbons and precursors (apical and basal) per hair cell
299 compared to controls (Figure 4-S2E,G-I). Interestingly, we observed slightly more complete
300 synapses per hair cell after a 16-hr taxol treatment (Figure 4-S2F). Overall, our long-term taxol
301 treatment indicated that microtubule stabilization did not dramatically impact synapse
302 formation in pLL hair cells.
303 Together, this pharmacology study revealed that long-term destabilization and
304 stabilization of microtubules during development can impact ribbon formation in pLL hair cells.
305 Microtubule destabilization had the most dramatic effect leading to more ribbons and
306 precursors, and the formation of fewer complete synapses.
307
308 ***Kif1aa* mutants have fewer synapses and more ribbon precursors**
309 For cargo (such as ribbons and precursors) to be transported along microtubules, molecular
310 motor proteins are required. Kinesin motor proteins transport cargo along microtubules
311 towards the growing, plus end. Our work demonstrated that in hair cells of the pLL, the plus
312 end of microtubules grow from the apex to the base of the cell (Figure 2). Single-cell RNA
313 sequencing (scRNAseq) has revealed that *kif1aa*, a zebrafish orthologue of mammalian Kif1a, a
314 plus-end directed kinesin motor protein, is highly expressed in pLL hair cells (Lush et al., 2019).
315 In zebrafish, there are 2 orthologues of mammalian *Kif1a*, *kif1aa* and *kif1ab*. ScRNA-seq in
316 zebrafish has demonstrated widespread co-expression of *kif1ab* and *kif1aa* mRNA in the
317 nervous system. Additionally, both scRNA-seq and fluorescent in situ hybridization have
318 revealed that pLL hair cells exclusively express *kif1aa* mRNA (David et al., 2024; Lush et al.,

319 2019; Sur et al., 2023). Therefore, we tested whether Kif1aa could be the kinesin motor that
320 transports ribbons and precursors to the cell base during development.
321 To test for the role of Kif1aa in pLL hair cells, we created a CRISPR-Cas9 mutant
322 (Varshney et al., 2016). Our *kif1aa* mutant has a stop codon in the motor domain and is
323 predicted to be a null mutation (Figure 5-S1A-B). Recent work in our lab using this mutant has
324 shown that Kif1aa is responsible for enriching glutamate-filled vesicles at the base of hair cells.
325 In addition, this work demonstrated that loss of Kif1aa results in functional defects in mature
326 hair cells including a reduction in evoked post-synaptic calcium responses (David et al., 2024).
327 We hypothesized that Kif1aa may also be playing an earlier role in ribbon formation.
328 For our initial analysis of *kif1aa* mutants, we co-labeled hair cells at 3 dpf with Ribeyeb
329 to label ribbons and precursors and pan-Maguk to label postsynapses (see examples: Figure 5A-
330 D). This is a similar endpoint used to examine synapse formation after our long-term
331 nocodazole and taxol treatments (Figure 4 and Figure 4-S2). We found that at 3 dpf *kif1aa*
332 mutants had a similar number of hair cells per neuromast (Figure 5E). Despite a similar number
333 of hair cells, we found that there were significantly fewer complete synapses per hair cell in
334 *kif1aa* mutants compared to controls (Figure 5F). In addition, we found that there were
335 significantly more ribbons and precursors (apical and basal) in *kif1aa* mutants compared to
336 controls (Figure 5G-I). As described in the previous section, we also observed fewer complete
337 synapses, and more ribbons and precursors after a 16-hr nocodazole treatment (Figure 4F-G).
338 Together, this suggests that both intact microtubules and Kif1aa are required for normal
339 synapse formation in pLL hair cells.
340
341 **Short-term disruption of microtubules, but not loss of Kif1aa, impacts ribbon formation**
342 Our initial experiments suggest that microtubule networks and Kif1aa are important for proper
343 synapse formation in pLL hair cells. However, the actual changes in precursors and ribbons
344 within developing hair cells was unclear. Therefore, we examined changes in ribbons and
345 precursors in living pLL hair cells over 3-4 hrs of development. For our analysis, we used
346 transgenic lines expressing YFP-tubulin to monitor microtubules and Riba-TagRFP to monitor

347 precursors and ribbons *in vivo*. We examined precursors and ribbons after nocodazole or taxol
348 treatment, or after knockdown of Kif1aa during this developmental window.
349 We verified the effectiveness of our *in vivo* pharmacological treatments using either 500
350 nM nocodazole or 25 µM taxol by imaging microtubule dynamics in pLL hair cells (*myo6b:YFP-*
351 *tubulin*). After a 30-min pharmacological treatment, we used Airyscan confocal microscopy to
352 acquire timelapses of YFP-tubulin (3 µm z-stacks, every 50-100 s for 30-70 min, Movie S8).
353 Compared to controls, 500 nM nocodazole destabilized microtubules (presence of
354 depolymerized YFP-tubulin in the cytosol, see arrows in Figure 4-S1F-G) and 25 µM taxol
355 dramatically stabilized microtubules (indicated by long, rigid microtubules, see arrowheads in
356 Figure 4-S1F,H) in pLL hair cells. We did still observe a subset of apical microtubules after
357 nocodazole treatment, indicating that this population is particularly stable (see asterisks in
358 Figure 4-S1F-H).
359 After verifying our *in vivo* pharmacological pharmacology treatments, we acquired
360 Airyscan confocal images of developing hair cells at 2 dpf that express YFP-tubulin and Riba-
361 TagRFP. Then after a 3-4 hr treatment in either 500 nM nocodazole or 25 µM taxol, we
362 reimaged the same hair cells. Consistent with our previous results (Figure 4 and Figure 4-S1,S2)
363 nocodazole and taxol treatments destabilized or stabilized microtubules respectively
364 (qualitative examples: Figure 6A-F). In each developing cell, we quantified the total number of
365 Riba-TagRFP puncta (apical and basal) before and after each treatment. In our control samples,
366 we observed on average no change in the number of Riba-TagRFP puncta per cell (Figure 6G).
367 Interestingly, we observed that nocodazole treatment led to a significant increase in the total
368 number of Riba-TagRFP puncta after 3-4 hrs (Figure 6G). This result is similar to our overnight
369 nocodazole experiments in fixed samples, where we also observed an increase in the number of
370 ribbons and precursors per hair cell. In contrast to our 3-4 hr nocodazole treatment, similar to
371 controls, taxol treatment did not alter the total number of Riba-TagRFP puncta over 3-4 hrs
372 (Figure 6G). Overall, our overnight and 3-4 hr pharmacology experiments demonstrate that
373 microtubule destabilization has a more significant impact on ribbon numbers compared to
374 microtubule stabilization.

375 Next, we used a similar approach to examine the number of Riba-TagRFP puncta in
376 *kif1aa* mutants over a 3-4 hr time window. For this analysis, we examined puncta in *kif1aa* F0
377 crispants. These mutants are derived from the injection of 2 *kif1aa* guide RNAs (gRNAs) and
378 Cas9 protein. This approach has shown to be an extremely effective way to assay gene function
379 in any genetic background (Hoshijima et al., 2019). Using this approach, we were able to
380 robustly disrupt the *kif1aa* locus (Figure 6-S1). We found that compared to uninjected controls,
381 in *kif1aa* F0 crispants there was no change in the total number of Riba-TagRFP puncta per cell
382 over 3-4 hrs (Figure 6-S2A-F). This result is slightly different than our analysis of *kif1aa* mutants
383 at 3 dpf where we observed significantly more ribbons and precursors per cell compared to
384 controls (Figure 5G). Overall, live imaging over a 3-4 hr time window indicates that a loss of
385 microtubule stability, but not loss of Kif1aa, results in an increase in Riba-TagRFP puncta within
386 developing pLL hair cells.
387
388 **Ribbons and precursors require microtubules, but not Kif1aa for directed motion**
389 Our tracking analyses revealed that ribbons and precursors show directed motion on
390 microtubules. Based on these results, we asked what happens to this movement if we disrupt
391 microtubules or the kinesin motor Kif1aa. To test whether microtubules are required for
392 directional ribbon and precursor motion, we used the drugs nocodazole and taxol to alter
393 microtubule dynamics. We treated the fish with these drugs for 30 min and recorded
394 timelapses of ribbon and precursor motion. This short treatment allowed us to observe ribbon
395 motion relatively soon after microtubule disruption and minimize any cytotoxic effects of the
396 compounds. Then we performed MSD and track displacement analyses on ribbon movement to
397 determine if directional motion was impaired (Figure 7A-B).
398 Using this approach we found that after destabilizing microtubules by treatment with
399 500 nM nocodazole for 30 min, the proportion of tracks with $\alpha > 1$ was significantly reduced
400 compared to controls (Figure 7C). In addition, we also found that the proportion of longer
401 tracks with a cumulative displacement > 1 µm was also reduced after nocodazole treatment
402 compared to controls (Figure 7F). This analysis indicates that an intact microtubule network is
403 needed for proper directional ribbon motion and longer displacements. In contrast, after

404 stabilizing microtubules by treatment with 25 µM taxol, we observed no effect on the
405 proportion of tracks with displacement > 1 µm or the proportion of tracks with $\alpha > 1$, compared
406 to controls (Figure 7D,G). Interestingly, when we examined the distribution of α values, we
407 observed that taxol treatment shifted the overall distribution towards higher α values (Figure 7-
408 S1A). In addition, when we plotted only tracks with directional motion ($\alpha > 1$), we found
409 significantly higher α values in hair cells treated with taxol compared to controls (Figure 7-S1B).
410 This indicates that in taxol-treated hair cells, where the microtubule network is stabilized,
411 ribbons with directional motion have higher velocities.
412 Next, we used a similar approach to examine the tracks of ribbon and precursor motion
413 in *kif1aa* mutants. For this analysis, we tracked ribbons and precursors in *kif1aa* F0 crispants.
414 We observed that the proportion of tracks with displacement > 1 µm was not significantly
415 different between *kif1aa* F0 crispants and controls (Figure 7H). Similarly, the proportion of
416 tracks with $\alpha > 1$, was also not significantly different from the controls (Figure 7E). Overall,
417 these tracking analyses show that in developing pLL hair cells, the kinesin motor Kif1aa is not
418 essential for the directional motion of ribbons and precursors. In contrast, an unperturbed
419 microtubule network is essential for directed motion.
420
421 **Ribbon precursors fuse on microtubules**
422 Our analyses demonstrate that the movement of ribbon precursors along microtubules is
423 important for synapse formation. But in addition to movement, during development it has been
424 proposed that these small precursors come together or fuse to form larger, more mature
425 ribbons (Michanski et al., 2019). This is consistent with our work, where we see a reduction in
426 ribbon and precursor numbers alongside development (Figure 1E). Further, we see an increase
427 in ribbon and precursor number when microtubules are destabilized (Figure 4), indicating an
428 intact microtubule network may also be important for ribbon fusion.
429 Consistent with this idea, in our timelapses, we observed that ribbons and precursors
430 undergo fusion on microtubules. These fusion events occurred between smaller precursors at
431 the cell apex as well as between larger precursors near the cell base (see examples: Figure 8A-
432 B, Figure 8-S1A-B, Movies S9-S11). We classified an event as a fusion once the ribbons could not

433 be resolved separately and stayed together for the length of the remaining timelapse (or at
434 least 5 min). Although we could not accurately measure the areas of precursors before and
435 after fusion, we did observe that the relative area resulting from the fusion of two smaller
436 precursors was greater than that of either precursor alone. This increase in area suggests that
437 precursor fusion may serve as a mechanism for generating larger ribbons (see examples: Figure
438 8-S1A-B). Fusion events usually involved ribbon precursors on two separate microtubule
439 filaments coming together during fusion, but fusion events could also occur on the same
440 filament. Although the fusion events were infrequent, within our time windows (30-70 min), we
441 quantified them and counted an average of 1.7 fusions and a maximum of 5 fusions events per
442 neuromast in developing pLL hair cells (n = 27 control neuromasts). Based on the close
443 association with microtubules during these events, we tested whether an intact microtubule
444 network was required for fusion events. We found that after treatment with 500 nM
445 nocodazole for 30 min, there were fewer fusions events (mean 0.4, maximum 2 fusions per
446 neuromast, n = 10 neuromasts). In contrast, the frequency of fusion events remained
447 unchanged upon treatment with 25 µM taxol for 30 min.
448 In our tracking analysis, we observed that Kif1aa was not required for the directional
449 motion of ribbon and precursors in developing hair cells (Figure 7E,H). However, our
450 immunohistological analyses indicated that there were more precursors and fewer complete
451 synapses in *kif1aa* mutants. Therefore, we examined whether Kif1aa was important for fusion
452 events. For this analysis, we quantified fusion events in *kif1aa* F0 crispants. We observed that
453 similar to nocodazole treatment, there were significantly fewer fusion events in *kif1aa* F0
454 crispants (mean 0.6, maximum 2 fusions per neuromast, n = 9 neuromasts). This reduction in
455 fusion events may ultimately account for the excess of precursors and fewer complete synapses
456 observed in *kif1aa* mutants (Figure 5). Together our results indicate that during development,
457 ribbon precursors can fuse when associated with microtubules, and an unperturbed
458 microtubule network, along with Kif1aa is needed for these fusion events.
459
460 **Discussion**

461 Our work in zebrafish applied high-resolution imaging approaches to investigate how ribbons
462 are assembled and mobilized in developing hair cells. Our study demonstrates that hair cells
463 have microtubule networks that are polarized with growing plus ends pointed to the cell base.
464 Live imaging highlights that during development, ribbons and precursors show directed motion
465 and fusion along microtubules and that an intact microtubule network is important for synapse
466 formation.
467
468 **Comparison of ribbon synapse formation in zebrafish and mice**
469 Compared to pLL hair cells (12-18 hrs), synapse formation and refinement occur over a
470 relatively long time window in mouse IHCs (E18-P14). In mice, much of the initial
471 synaptogenesis occurs embryonically, while synapse refinement and pruning occur later,
472 during the first postnatal week. Due to the rapid time course of synapse development in
473 zebrafish, our experiments likely encompass ribbon precursor movement during
474 synaptogenesis and synapse refinement. The companion paper on mouse IHCs focused
475 primarily on ribbon mobility during the dramatic pruning of synapses that occurs during early
476 postnatal development (Voorn et al., 2024). Unfortunately, it was not possible to study earlier
477 events in mouse IHCs, as equivalent experiments were not possible embryonically. Live imaging
478 at postnatal stages in mice indicates that during synapse pruning in IHCs, ribbons may detach
479 from the membrane, undergo local trafficking, and fuse to nearby presynaptic AZs. Together
480 our studies in zebrafish and mouse hair cells illuminate several common features that
481 characterize ribbon and microtubule dynamics during synapse formation.
482 First, immunostaining in both zebrafish and mice revealed an extensive network of
483 microtubules within hair cells. In both species, the majority of microtubules were stabilized by
484 tubulin acetylation (Figure 2-S1). Our *in vivo* imaging of EB3-GFP in zebrafish hair cells revealed
485 that microtubules are very dynamic, and the plus ends of microtubules grow towards the cell
486 base, towards the presynaptic AZ (Figure 2). This data is consistent with data in mouse IHCs
487 demonstrated via immunostaining that the minus end marker of microtubules, CAMSAP2,
488 localizes to the IHC apex (Vorn et. al.). Overall, both studies demonstrate that microtubule
489 networks in developing hair cells are polarized with the plus ends pointed to the cell base.

490 Second, live imaging in zebrafish and mouse hair cells revealed that ribbons associate
491 with and move along microtubules. Tracking and quantification of ribbon movement via MSD
492 analysis revealed that in both zebrafish and mouse hair cells, the majority of ribbons show
493 motion indicative of confinement (Figure 3, $\alpha < 1$). In addition, a subset of ribbon tracks shows
494 evidence of directed motion (Figure 3, $\alpha > 1$, or displacements > 1 µm). In both species, after
495 using nocodazole to destabilize microtubules, there was a dramatic reduction in instances of
496 directed motion (Figure 7). In addition to ribbon movement, ribbon fusion was observed in the
497 hair cells of mice and zebrafish (Figure 8). Interestingly, in mice many fusion events were
498 balanced out by divisions, or ribbons undergoing separation. In contrast, ribbon divisions were
499 not prevalent in zebrafish hair cells. A lack of ribbon divisions could be due to the rapid speed of
500 development in zebrafish hair cells, where divisions are too transient in nature to be confirmed.
501 Alternatively, divisions may occur primarily late in synapse development and these events were
502 overall less abundant in our zebrafish datasets. Importantly, in both mouse and zebrafish hair
503 cells, ribbon fusion was diminished after microtubule destabilization. Together these results in
504 mice and zebrafish demonstrate that an intact microtubule network is required for the directed
505 motion and fusion of ribbons during development.
506 Third, we sought to explore the kinesin motor responsible for ribbon movement in hair
507 cells using zebrafish and mouse models. Based on scRNAseq data and previous immunostaining
508 evidence we focused on Kif1a (Lush et al., 2019; Michanski et al., 2019). In both mouse *Kif1a*
509 and zebrafish *kif1aa* mutants, a common observation was an overall reduction in ribbon size
510 (Figure 5). This suggests that a conserved mechanism where both intact microtubules and
511 Kif1aa are required for normal ribbon formation. Despite these results, future work in zebrafish
512 and mice is needed to explore additional kinesin motors that can drive ribbon movement
513 during synapse formation.
514
515 **Fusion on microtubules as a mechanism for ribbon enlargement and maturation**
516 Numerous studies have documented small ribbon precursors in developing photoreceptors and
517 hair cells; later in development there are fewer, large ribbons present (Michanski et al., 2019;
518 Regus-Leidig et al., 2009; Schmitz, 2009; Sheets et al., 2011; Sobkowicz et al., 1986, 1982). This

519 has led to the hypothesis that ribbon precursor fusion is a mechanism to form larger, more
520 mature ribbons (Michanski et al., 2019). Our live imaging experiments show that ribbon fusion
521 is indeed a feature of ribbon formation (Figure 8, Figure 8-S1). Interestingly, we observed that
522 fusion often occurs between precursors on adjacent microtubules. Fusion events can occur
523 both apically and basally within hair cells. More apical fusion events are likely a way to increase
524 ribbon size early in development. More basal fusion events could represent the synapse
525 reduction and refinement that occurs later in synapse development. Whether these later, basal
526 fusion events occur after postsynaptic elements are present is unclear and awaits additional
527 studies. Importantly we found that the number of fusion events decreased when microtubule
528 networks were disrupted or when Kif1aa was absent (Figure 8). Together these results confirm
529 the hypothesis that ribbons fuse during development. In addition, our work demonstrates that
530 microtubules and Kif1aa are necessary for fusion and may help facilitate this process.
531 Ribbons are aggregates of proteins that share many features with biomolecular
532 condensates that form through liquid-liquid phase separation (LLPS) (Wang et al., 2021).
533 Biomolecular condensates are nano- to micro-meter scale compartments that function to
534 concentrate proteins and nucleic acids. Some examples of biomolecular condensates include
535 tight junctions, postsynaptic densities, ribonucleoprotein (RNP) granules, and stress granules
536 (Wang et al., 2021; Wiegand and Hyman, 2020). These condensates are highly mobile and
537 dynamic and constituent molecules diffuse readily and exchange with the surrounding
538 environment. Biomolecular condensates often undergo fusion to form larger ones, and then
539 shrink into a spherical shape (Wiegand and Hyman, 2020). FRAP analyses of Ribeye-GFP labeled
540 ribbons in hair cells have confirmed that tagged Ribeye has a fast recovery phase within
541 ribbons, verifying that Ribeye is highly mobile and dynamic within ribbons (Graydon et al.,
542 2017). Further, these FRAP studies revealed that Ribeye molecules can exchange with the
543 surrounding environment. Our present studies confirmed that ribbon precursors undergo
544 fusion to form larger spherical ribbons (Figure 8A,B). Together these studies point towards the
545 idea that precursors and ribbons are indeed biomolecular condensates. Ribeye also contains
546 sequences predicted to be intrinsically disordered, a feature of molecules that can mediate
547 condensate formation. Interestingly, several biomolecular condensates such as RNP transport

548 granules are known to be transported along the microtubules (Knowles at al., 1996), similar to
549 our observations of ribbon precursor transport.
550 In our current study, we also found that microtubules are needed for fusion (Figure 8C).
551 In other cellular contexts, the energy released by dynamic microtubules via growth and
552 shrinkage can be used for force generation in a wide range of processes (Vleugel et al., 2016).
553 Interestingly, work on stress granule condensates found a connection between dynamic
554 microtubules and stress granule formation. This work demonstrated that microtubule growth
555 and shrinkage promoted the fusion of small cytoplasmic granules into larger ones (Chernov et
556 al., 2009). In addition, this study also demonstrated that stress granules slide along
557 microtubules and that this movement may act in conjunction with pushing or pulling to
558 promote fusion (Chernov et al., 2009). Ribbons and microtubules may also interact during
559 development to promote fusion. Disrupting microtubules could interfere with this process,
560 preventing ribbon maturation. Consistent with this, short-term (3-4 hr) and long-term
561 (overnight) nocodazole increased ribbon and precursor numbers (Figure 6AG; Figure 4G),
562 suggesting reduced fusion. Long-term treatment (overnight) resulted in a shift toward smaller
563 ribbons (Figure 4H-I), and ultimately fewer complete synapses (Figure 4F).
564 We also observed that fusion was disrupted in *kif1aa* mutants, despite finding that
565 directed transport of precursors and ribbons remained unchanged in *kif1aa* mutants (Figure
566 7,8). A recent study on RNP condensates examined kinesin motors and adaptors in the context
567 of microtubules (Cochard et al., 2023). This work found that the precise combination of motor
568 proteins or adaptors can impact where condensates form. Some combinations enabled the
569 formation and transport of condensates along microtubules. However, other combinations
570 restricted condensate formation to microtubule terminals where motor proteins are predicted
571 to form a scaffold. Our work indicates that while more than one kinesin motor protein is
572 capable of transporting ribbon precursors, it is predominantly Kif1aa that mediates fusion along
573 microtubules. This could explain why precursor fusion, but not transport is impacted in *kif1aa*
574 mutants (Figure 7,8). This scenario could also account for the increased number of precursors
575 and the reduced number of complete synapses observed in *kif1aa* mutants (Figure 5).
576

577 **Kinesin motors and adaptors for ribbon transport on microtubules**

578 Our immunohistochemistry analyses show clear synaptic defects in *kif1aa* mutants after the
579 bulk of synapse formation has occurred (fewer synapses, more precursors, Figure 5). Despite
580 these defects, we were unable to demonstrate that loss of Kif1aa impacts the movement of
581 precursors along microtubules (Figure 7). These results suggest that another kinesin motor may
582 function to transport precursors and ribbons. Pulldown assays have shown an interaction of
583 Kif3a with Ribeye (Uthaiah and Hudspeth, 2010). While *kif1aa* mRNA is the most abundant
584 kinesin motor protein transcript detected in pLL hair cells, *kif3a* mRNA is also present. *Kif3a*
585 mRNA is present at lower levels and is expressed more broadly in pLL hair cells, supporting
586 cells, and afferent neurons (Sur et al., 2023). Therefore, both Kif1aa and Kif3a may be
587 competent to transport developing ribbons. Future work exploring the role of Kif3a separately
588 or in combination with Kif1aa will illuminate the role these motors play in synapse assembly in
589 hair cells. In addition, it will be useful to visualize these kinesins by fluorescently tagging them
590 in live hair cells to observe whether they associate with ribbons.

591 Regardless of the anterograde kinesin motor(s) that transports precursors to the cell
592 base, we also observed that precursors can also move in the retrograde direction, towards the
593 cell apex (Figure 3C bottom panels, Figure 3L, and Figure 3-S1B). In fact, out of the tracks with
594 directional motion, we found that 20.8 % of precursors moved apically. This could be due to the
595 fact that a subpopulation of microtubules shows plus-end mediated growth apically (22.8 %).
596 Alternatively, it is possible that retrograde motors may also transport ribbon precursors. For
597 example, this could be accomplished using minus-end directed motors, such as cytoplasmic
598 dynein heavy chain, or kinesins in the kinesin-14 family (Sweeney and Holzbaur, 2018; Yamada
599 et al., 2017). In the future, it will be important to explore the role of these additional motor
600 proteins in the context of ribbon and precursor mobility.

601 Our findings indicate that ribbons and precursors show directed motion indicative of
602 motor-mediated transport (Figure 3 and 7). While a subset of ribbons moves directionally with
603 α values > 1, canonical motor-driven transport in other systems, such as axonal transport, can
604 achieve even higher α values approaching 2 (Bellotti et al., 2021; Corradi et al., 2020). We
605 suggest that relatively lower α values arise from the highly dynamic nature of microtubules in

606 hair cells. In axons, microtubules form stable, linear tracks that allow kinesins to transport cargo
607 with high velocity. In contrast, the microtubule network in hair cells is highly dynamic,
608 particularly near the cell base. Within a single time frame (50-100 s), we observe continuous
609 movement and branching of these networks. This dynamic behavior adds complexity to ribbon
610 motion, leading to frequent stalling, filament switching, and reversals in direction. As a result,
611 ribbon transport appears less directional than the movement of traditional motor cargoes along
612 stable axonal filaments, resulting in lower α values compared to canonical motor-mediated
613 transport. Notably, treatment with taxol, which stabilizes microtubules, increased α values to
614 levels closer to those observed in canonical motor-driven transport (Figure 7-S1). This finding
615 supports the idea that the relatively lower α values in hair cells are a consequence of a more
616 dynamic microtubule network. Overall, this dynamic network gives rise to a slower, non-
617 canonical mode of transport.
618 Another important component of motor-mediated transport is adaptor proteins that
619 selectively link cargo to specific motor proteins (Fu and Holzbaur, 2014). In neurons, cargos
620 leave the Golgi apparatus and are packed into specialized transport vesicles, along with adaptor
621 scaffolds (Farías et al., 2012; Sampo et al., 2003). Work in neurons has shown that the Kif1a
622 motor transports Rab3-positive synaptic vesicle precursors (Okada et al., 1995). This transport
623 is thought to rely on DENN (differentially expressed in normal and neoplastic cells)/MADD (MAP
624 kinase activating death domain) which links synaptic vesicle precursors to Kif1a (Hummel and
625 Hoogenraad, 2021; Niwa et al., 2008). Interestingly, like mature ribbons, ribbon precursors are
626 decorated with synaptic vesicles (Michanski et al., 2019). Thus, is it possible that these synaptic
627 vesicles may contain adaptor proteins that couple the ribbon to a kinesin motor to enable
628 transport. In the future, it will be important to identify this adaptor protein and to understand
629 what other molecules are co-transported with Ribeye during ribbon formation.
630
631 **Ribbon formation in the absence of microtubules**
632 Our work indicates that over short time scales (30-70 min), microtubule destabilization via
633 nocodazole treatment reduces the number of ribbons and precursors that show directed
634 motion indicative of active transport (Figure 7). In addition, prolonged nocodazole treatment

635 throughout development (16 hrs) leads to the formation of fewer synapses (Figure 4). But in
636 both treatment paradigms, some ribbons still show directed motion, and some synapses
637 continue to form despite microtubule disruption. If tracks of microtubules are required for
638 developing precursor and ribbon mobility during development, what underlies this residual
639 movement and synapse formation?

640 One possibility is that not all microtubules are disrupted after nocodazole treatment.
641 While high doses of nocodazole (~40 µM) eliminate all microtubules, they are also cytotoxic
642 (Laisne et al., 2021). The doses used in our experiments (100-500 nM) were not cytotoxic,
643 although higher doses did result in the death of hair cells. At these lower doses, microtubules—
644 especially the more apical, stable population (see examples: Figure 2-S1B, Figure 4-S1F-G)—
645 were not entirely disrupted. Residual ribbon mobility during nocodazole treatment could occur
646 along these remaining microtubules. Alternatively, other cytoskeletal components, such as
647 actin or intermediate filaments may contribute to ribbon mobility. Work in mouse IHCs has
648 shown that actin filaments help regulate and organize synaptic vesicles at mature ribbon
649 synapses (Guillet et al., 2016). In addition, in mice, the actin-based motor protein Myosin6 has
650 been implicated in ribbon-synapse formation and function (Roux et al., 2009). A third possibility
651 is that ribbons and precursors move through the cytoplasm via diffusion and are captured at
652 the AZ via an adapter protein. Although we primarily observed ribbons and precursors attached
653 to microtubules, when these filaments are destabilized using nocodazole, movement could still
654 occur via diffusion. Once near the base of the cell, presynaptic molecules such as Bassoon,
655 could act to anchor ribbons at the AZ (Jing et al., 2013). Any of these scenarios—residual
656 microtubule-based transport, alternative cytoskeletal component, or diffusion followed by
657 capture—could explain how ribbons continue to move and how synapses still form in the
658 absence of intact microtubules. In all likelihood, a combination of these processes is required to
659 ensure that ribbon synapses form properly. Additional pharmacological and imaging
660 experiments are needed to delineate the relative contributions of these processes.

661 Another important consideration is the potential off-target effects of nocodazole. Even
662 at non-cytotoxic doses, nocodazole toxicity may impact ribbons and synapses independently of
663 its effects on microtubules. While this is less of a concern in the short- and medium-term

664 experiments (30 min to 4 hr), long-term treatments (16 hrs) could introduce confounding
665 effects. Additionally, nocodazole treatment is not hair cell-specific and could disrupt
666 microtubule organization within afferent terminals as well. Thus, the reduction in ribbon-
667 synapse formation following prolonged nocodazole treatment may result from microtubule
668 disruption in hair cells, afferent terminals, or a combination of the two.
669
670 **Does spontaneous activity shape ribbon transport or fusion?**
671 In previous work, we demonstrated that spontaneous calcium activity impacts ribbon formation
672 in pLL hair cells (Sheets et al., 2012; Wong et al., 2019). Spontaneous activity is well
673 documented in developing sensory systems [reviewed in: (Leighton and Lohmann, 2016)]. In
674 the inner ear of mammals, spontaneous activity in sensory hair cells is thought to act during
675 development to establish neuronal connections within the inner ear, and downstream in the
676 brain to shape tonotopic maps (Ceriani et al., 2019; Tritsch et al., 2007). In our previous work in
677 pLL hair cells, we found that spontaneous rises in presynaptic calcium loads calcium into
678 synaptic mitochondria. Calcium loading into the mitochondria regulates the amount of NAD^+ to
679 NAD(H) in the developing hair cell. Blocking either presynaptic or mitochondria calcium during
680 development results in higher levels of NAD^+, the formation of larger ribbons, fewer synapses,
681 and the retention of small ribbon precursors in hair cells (Sheets et al., 2012; Wong et al.,
682 2019). What aspect of ribbon formation is impacted by spontaneous activity remains unclear.
683 Work in yeast has shown that calcium is important for microtubule stability (Adamíková
684 et al., 2004; Façanha et al., 2002). In addition, work in dendritic spines has shown that synaptic
685 calcium responses promote microtubule entry into active spines (Merriam et al., 2013).
686 Therefore, it is possible that spontaneous calcium activity may act to stabilize microtubules or
687 facilitate movement to the presynaptic AZ to facilitate ribbon transport. In addition to altering
688 the microtubule network, spontaneous activity could also impact ribbon fusion. Protein
689 condensate formation and fusion are influenced by many aspects of the cellular environment,
690 including temperature, pH, osmolarity, and ion concentration (Wang et al., 2022). Elevated
691 calcium can promote the fusion of chromogranin proteins that undergo LLPS in the Golgi lumen
692 (Gerdes et al., 1989; Yoo, 1995). Therefore, it is possible that elevated calcium during a

693 spontaneous calcium event could promote ribbon or precursor fusion. In addition to the cellular
694 environment, posttranslational modifications to the proteins within the condensate can impact
695 formation and LLPS. Such modifications include: phosphorylation, acetylation, SUMOylation,
696 ubiquitination, methylation, and ADP-ribosylation (Luo et al., 2021). These modifications can
697 alter protein-protein interactions by changing the charge, structure, or hydrophobicity. Our
698 previous work indicated that NAD^+ or NAD(H) via a NAD^+/NADH binding domain on Ribeye
699 impacts ribbon formation (Wong et al., 2019). It is possible that in addition to calcium,
700 NAD^+/NADH levels in the cell could modify Ribeye to facilitate condensate formation or fusion.
701 In the future, it will be important to use the live imaging approaches outlined here to
702 understand how spontaneous presynaptic- and mitochondrial-calcium influx impact the
703 movement and fusion of ribbon precursors.
704
705 Overall, our live imaging studies demonstrate that microtubule networks are critical for ribbon
706 and precursor mobility, and fusion in developing zebrafish hair cells. However, ribbon synapses
707 contain many molecules, and synapse formation requires many successive steps. In the future it
708 will be important to develop approaches to endogenously tag and label other presynaptic
709 ($Ca_V1.3$ channels, Bassoon, Piccolino) and postsynaptic proteins (PSD95, GluR2/3/4) that make
710 up ribbon synapses. For this future work, zebrafish is an ideal model system for creating these
711 new genetic tools and for live imaging. By imaging ribbons, along with these other tagged
712 synaptic components, we will gain a more comprehensive picture of synapse formation.
713 Understanding how ribbon synapses form is essential to determining how to reform synapses
714 when they are disrupted in auditory and visual disorders.
715
716 **Methods**
717 **Zebrafish animals**
718 Zebrafish (*Danio rerio*) were bred and cared for at the National Institutes of Health (NIH) under
719 animal study protocol #1362-13. Zebrafish larvae were raised at 28°C in E3 embryo medium
720 (5 mM NaCl, 0.17 mM KCl, 0.33 mM $CaCl_2$, and 0.33 mM $MgSO_4$, buffered in HEPES, pH 7.2).
721 All experiments were performed on larvae aged 2-5 days post fertilization (dpf). Larvae were

722 chosen at random at an age where sex determination is not possible. The previously described
723 mutant and transgenic lines were used in this study: *Tg(myo6b:ctbp2a-TagRFP)*^{idc11Tg} referred to
724 as *myo6b:riba-TagRFP; Tg(myo6b:YFP-Hsa.TUBA)*^{idc16Tg} referred to as *myo6b:YFP-tubulin* (Ohta
725 et al., 2020; Wong et al., 2019). *Tg(myo6b:ctbp2a-TagRFP)*^{idc11Tg} reliably labels mature ribbons,
726 similar to a pan-CTBP immunolabel at 5 dpf (Figure 1-S1A-B). This transgenic line does not alter
727 the number of hair cells or complete synapses per hair cell (Figure 1-S1A-D). In addition,
728 *myo6b:ctbp2a-TagRFP* does not alter the size of ribbons (Figure 1-S1E).
729
730 **Zebrafish transgenic and CRISPR-Cas9 mutant generation**
731 To create *myo6b:EB3-GFP* transgenic fish, plasmid construction was based on the tol2/gateway
732 zebrafish kit (Kwan et al., 2007). The p5E *pmyo6b* entry clone (Trapani et al., 2009) was used to
733 drive expression in hair cells. A pME-*EB3-GFP* clone was kindly provided by Catherine Drerup at
734 the University of Wisconsin, Madison. pDestTol2pACryGFP was a gift from Joachim Berger &
735 Peter Currie (Addgene plasmid # 64022). These clones were used along with the following tol2
736 kit gateway clone, p3E-*polyA* (#302) to create the expression construct: *myo6b:EB3-GFP*. To
737 generate the stable transgenic fish line *myo6b:EB3-GFP*^{idc23Tg}, plasmid DNA and tol2
738 transposase mRNA were injected into zebrafish embryos as previously described (Kwan et al.,
739 2007). The *myo6b:EB3-GFP*^{idc23Tg} transgenic line was selected for a single copy and low
740 expression of EB3-GFP.
741 A *kif1aa* germline mutant (*kif1aa*^{idc24}*)* was generated using CRISPR-Cas9 technology as
742 previously described (Varshney et al., 2016). Exon 6, containing part of the Kinesin motor
743 domain was targeted (Figure 5-S1A). Guides RNAs (gRNAs) targeted to *kif1aa* are as follows: 5'-
744 ACGGATGTTCTCGCACACGT(AGG)-3', 5'-GTGCGAGAACATCCGTTGCT(AGG)-3', 5'-
745 TGGACTCCGGGAATAAGGCT(AGG)-3', 5'-AGAATACCTAGCCTTATTCC(CGG)-3'. Founder fish were
746 identified using fragment analysis of fluorescent PCR (fPCR) products. A founder fish containing
747 a complex insertion or deletion (INDEL) that destroys a BslI restriction site in exon 6 was
748 selected (Figure 5-S1B). This INDEL disrupts the protein at amino acid 166 (Figure 5-S1A).
749 Subsequent genotyping was accomplished using standard PCR with touchdown, and BslI

750 restriction enzyme digestion. *Kif1aa* genotyping primers used were: *kif1aa*_FWD 5'-
751 AACACCAAGCTGACCAGTGC-3' and *kif1aa*_REV 5'-TGCGGTCCTAGGCTTACAAT-3'.
752 Because *kif1aa* mutants have no phenotype to distinguish them from sibling controls at
753 the ages imaged, the low throughput of our live imaging approaches made using germline
754 mutants prohibitive. Therefore, we created *kif1aa* F0 crispants for our live imaging analyses.
755 Here we injected the following *kif1aa* gRNAs: 5'-GTGCGAGAACATCCGTTGCT(AGG)-3' and 5'-
756 AGAATACCTAGCCTTATTCC(CGG)-3', along with Cas9 protein, as previously described (Hoshijima
757 et al., 2019). We then grew *kif1aa* injected F0 crispants for 2 days and then used them for our
758 live imaging analyses. Studies have shown that F0 crispants are a fast and effective way to
759 knock down gene function in any genetic background (Hoshijima et al., 2019; Sheets et al.,
760 2021). After live imaging, we genotyped all *kif1aa* F0 crispants (Figure 6-S1) to ensure that the
761 gRNAs cut the target robustly using fPCR and the following primers: *kif1aa*_FWD_fPCR 5'-
762 TGTAAAACGACGGCCAGT-AAATAGAGATTCACTTTTAATC-3' and *kif1aa*_REV_fPCR 5'- GTGTCTT-
763 CCTAGGCTTACAATGCTTTTGG-3' (Carrington et al., 2015). fPCR fragments were run on a genetic
764 analyzer (Applied Biosystems, 3500XL) using LIZ500 (Applied Biosystems, 4322682) as a dye
765 standard. Analysis of fPCR revealed an average peak height of 4740 a.u. in wild type, and an
766 average peak height of 126 a.u. in *kif1aa* F0 crispants (Figure 6-S1E-F). Any *kif1aa* F0 crispant
767 without robust genomic cutting or a peak height > 500 a.u. was not included in our analyses.
768
769 **Zebrafish pharmacology**
770 To destabilize or stabilize microtubules, larval zebrafish at 2 dpf were incubated in either
771 nocodazole (Sigma-Aldrich, SML1665) or Paclitaxel (taxol) (Sigma-Aldrich, 5082270001). Both
772 drugs were maintained in DMSO. For experiments these drugs were diluted in media for a final
773 concentration of 0.1 % DMSO, 250-500 nM nocodazole, and 25 µM taxol. For controls, larvae
774 were incubated in media containing 0.1 % DMSO. For long-term incubation (16 hr), wild-type
775 larvae were incubated in E3 media containing 250 nM nocodazole or 25 µM taxol at 54 hpf for
776 16 hrs (overnight). After this long-term treatment, larvae were fixed and prepared for
777 immunohistochemistry (see below). For live, short-term incubations (for 3-4 hr incubations or
778 ribbon tracking), transgenic larvae (*myo6b:riba-tagRFP; Tg(myo6b:YFP-alpha-tubulin*) at 48-54

779 hpf were embedded in 1 % low melt agarose prepared in E3 media containing 0.03 % tricaine
780 (Sigma-Aldrich, A5040, ethyl 3-aminobenzoate methanesulfonate salt). 500 nM nocodazole, 25
781 µM taxol, or DMSO were added to the agarose and to the E3 media used to hydrate the sample.
782 For short-term treatments, hair cells were imaged after 30 min of embedding.
783
784 **Immunohistochemistry of zebrafish samples**
785 Immunohistochemistry used to label acetylated-α-tubulin, tyrosinated-α-tubulin, Ribeyeb or
786 pan-CTBP (ribbons and precursors), pan-Maguk (postsynaptic densities), and Myosin7a (cell
787 bodies) was performed on whole zebrafish larvae similar to previous work. The following
788 primary antibodies were used: rabbit anti-Myosin7a (Proteus 25-6790; 1:1000); mouse anti-
789 pan-Maguk (IgG1) (Millipore MABN7; 1:500); mouse anti-Ribeyeb (IgG2a) ((Sheets et al., 2011);
790 1:10,000); mouse anti-CTPB (IgG2a) (Santa Cruz sc-55502; 1:1000); mouse anti-acetylated-α-
791 tubulin (IgG2b) (Sigma-Aldrich T7451; 1:5,000); mouse anti-tyrosinated-α-tubulin (IgG2a)
792 (Sigma-Aldrich MAB1864-I; 1:1,000); chicken anti-GFP (to stain YFP-tubulin) (Aves labs GFP-
793 1010; 1:1,000). The following secondary antibodies were used at 1:1,000: (ThermoFisher
794 Scientific, A-11008; A-21143, A-21131, A-21240; A-11-039, A-21242, A-21241, A-11039). Larvae
795 were fixed with 4 % paraformaldehyde in PBS for 4 hr at 4°C. All wash, block, and antibody
796 solutions were prepared in 0.1 % Tween in PBS (PBST). After fixation, larvae were washed 5 × 5
797 min in PBST. Prior to block, larvae were permeabilized with acetone. For this permeabilization
798 larvae were first washed for 5 min with H_2O. The H_2O was removed and replaced with ice-cold
799 acetone and samples were placed at −20°C for 3 min, followed by a 5 min H_2O wash. The larvae
800 were then washed for 5 × 5 min in PBST. Larvae were then blocked overnight at 4°C in blocking
801 solution (2 % goat serum, 1 % bovine serum albumin, and 2 % fish skin gelatin in PBST). Larvae
802 were then incubated in primary antibodies in antibody solution (1 % bovine serum albumin in
803 PBST) overnight, nutating at 4°C. The next day, the larvae were washed for 5 × 5 min in PBST to
804 remove the primary antibodies. Secondary antibodies in antibody solution were added and
805 larvae were incubated for 3 hrs at room temperature. After 5 × 5 min washes min in PBST to
806 remove the secondary antibodies, larvae were rinsed in H_2O and mounted in Prolong gold
807 (ThermoFisher Scientific, P36930).

808

809 **Confocal imaging and analysis of fixed zebrafish samples**

810 After immunostaining, fixed zebrafish samples were imaged on an inverted Zeiss LSM 780 (Zen
811 2.3 SP1) or an upright Zeiss LSM 980 (Zen 3.4) laser-scanning confocal microscope with Airyscan
812 using a 63x 1.4 NA oil objective lens. Z-stacks encompassing the entire neuromast were
813 acquired every 0.17 (LSM 980) or 0.18 (LSM 780) µm with an 0.04 µm x-y pixel size and Airyscan
814 autoprocessed in 3D.

815 Synaptic images from fixed samples were further processed using FIJI. Acetylated-α-
816 tubulin or Myosin7 label was used to manually count hair cells. Complete synapses comprised
817 of both a Ribeyeb/CTBP and Maguk puncta were also counted manually. To quantify the area of
818 each ribbon and precursor, images were processed in FIJI using a macro,
819 'IJMacro_AIRYSCAN_simple3dSeg_ribbons only.ijm' as previously described (Wong et al., 2019).
820 Here each Airyscan z-stack was max-projected, and background corrected using rolling-ball
821 subtraction. A threshold was applied to each image, followed by segmentation to delineate
822 individual Ribeyeb/CTBP puncta. The watershed function was used to separate adjacent puncta.
823 A list of 2D objects of individual ROIs (minimum size filter of 0.002 μm^2) was created to measure
824 the 2D areas of each Ribeyeb/CTBP puncta. Areas for all Ribeyeb/CTBP puncta within each
825 neuromast were then exported as a csv spreadsheet. Areas were averaged per neuromast, per
826 genotype or plotted in a frequency distribution. For comparisons, all fixed images analyzed in
827 FIJI were imaged and processed using the same parameters.

828 To quantify the mean intensity of acetylated-α-tubulin after overnight nocodazole or
829 taxol treatments, 20 slices centered on the hair cells were max-projected in FIJI. An ROI was
830 drawn around the hair cells, and this ROI was used to measure the mean intensity of the
831 acetylated-α-tubulin label in each neuromast.

832

833 **Confocal imaging and *in vivo* analysis of ribbon numbers in developing zebrafish hair cells**

834 For counting ribbon numbers in developing and mature hair cells (Figure 1), double transgenic
835 *myo6b:riba-TagRFP* and *myo6b:YFP-tubulin* larvae at 2 and 3 dpf were imaged. Transgenic
836 larvae were pinned to a Sylgard-filled petri dish in E3 media containing 0.03 % tricaine and

837 imaged on a Nikon A1R upright confocal microscope using a 60x 1 NA water objective lens.
838 Denoised images were acquired using NIS Elements AR 5.20.02 with an 0.425 µm z-interval, at,
839 16x averaging, and 0.05 µm/pixel. Z-stacks of whole neuromasts including the kinocilium were
840 acquired in a top-down configuration using 488 and 561 nm lasers. The 488 nm laser along with
841 a transmitted PMT (T-PMT) detector was used to capture the kinocilial heights.
842 For the quantification of ribbon numbers at different developmental stages (Figure 1), a
843 custom-written Fiji macro "Live ribbon counter" was used to batch-process the z-stacks. The
844 red channel (Riba-TagRFP) of each z-stack was thresholded (threshold value = 97). Watershed
845 was applied to the thresholded stack to separate ribbons near each other. The resulting mask
846 from the thresholding and watershedding was applied to the original red channel. The number
847 of ribbons was then counted using '3D Objects Counter' plugin (Threshold = 1, min size = 0, max
848 size = 183500). The counted objects were merged with the green channel (YFP-tubulin). Each z-
849 stack was visually inspected to determine the localization of the ribbons. Ribbons below the
850 nucleus were classified as 'basal' and the rest as 'apical'. The number of apical and basal
851 ribbons was counted in each hair cell.
852 To classify the developmental stage of each hair cell (Figure 1), the height of the
853 kinocilium was used. The number of z-slices between the kinocilium tip and base was
854 determined and multiplied by the z-slice interval (0.425 µm) to get the kinocilium height. Hair
855 cells with heights < 1.5 µm were classified as 'early', hair cells with heights 1.5-10 µm were
856 classified as 'intermediate' and hair cells with heights 10-18 µm were classified as 'late'. Hair
857 cells with heights > 18 µm were considered 'mature'.
858
859 **Confocal imaging and *in vivo* tracking EB3-GFP dynamics in zebrafish**
860 Transgenic *myo6b:EB3-GFP* larvae at 2-3 dpf were mounted in 1 % LMP agarose containing 0.03
861 % tricaine in a glass-bottom dish. Larvae were imaged on an inverted Zeiss LSM 780 (Zen 2.3
862 SP1) confocal microscope using a 63x 1.4 NA oil objective lens. For timelapses, confocal z-stacks
863 of partial cell volumes (3.5 µm, 7 z slices at 0.5 µm z interval) with an 0.07 µm x-y pixel size
864 were taken every 7 s for 15-30 min.

865 The EB3-GFP timelapses were registered in FIJI using the plugin "Correct 3D drift"
866 (Parslow et al., 2014), max-projected, and then tracked in 2D in Imaris. For spot detection, we
867 used an estimated xy diameter of 0.534 µm with background subtraction. The detected spots
868 were filtered by 'Quality' using the automatic threshold. The timelapses were visually checked
869 to make sure the spot detection was accurate. For the tracking step, the 'Autoregressive
870 motion' algorithm was used, with a maximum linking distance of 1 µm and a maximum gap size
871 of 3 frames. To ensure accurate track detection, short tracks were removed by filtering for the
872 number of spots in a track (> 5) and track displacement length (> automatic threshold).
873 To calculate the track angles relative to the cell base, we used cells that lie horizontally
874 so we only need to consider the angles in the 2D, xy plane. In Imaris, the tracks in each hair cell
875 were selected and exported separately. Using the start and end position coordinates of the
876 exported tracks, we calculated track angles in MATLAB using custom-written code called, "EB3
877 track angle". The angle of each hair cell was measured in Imaris. The final track angle
878 distribution plotted was obtained by measuring the difference between each track angle and
879 the angle of the hair cell.
880 To create movies of EB3-GFP tracks in Movie S1, the FIJI plugin "Correct 3D drift" was
881 applied to the timelapse. Z-stacks were then max-projected, and tracks were detected using the
882 FIJI plugin TrackMate (Parslow et al., 2014; Tinevez et al., 2017). For Movie S1, the LoG detector
883 in TrackMate was used with an estimated object diameter of 0.6 µm, and a quality threshold of
884 8, using a median filter and sub-pixel localization. The Linear Assignment Problem (LAP) tracker
885 was selected using a frame to frame linking max distance of 1 µm, a track segment gap closing
886 max distance of 1 µm and a max frame gap of 2 µm. Tracks were colored by Track index. For
887 viewing tracks over time, tracks were displayed as "Show tracks backwards in time" with a fade
888 range of 5-time points. To create a color-coded temporal map of EB3-GFP tracks over a short
889 time window (21 s, Figure 2C-D), the FIJI Hyperstack plugin "Temporal-Color code" was used
890 with the 16 colors LUT.
891
892 **Confocal imaging and *in vivo* analysis of ribbon numbers after short-term pharmacological**
893 **treatments in zebrafish**

894 For counting ribbons after 3-4 hr drug treatment, transgenic zebrafish expressing *myo6b:riba-*
895 *TagRFP* and *myo6b:YFP-tubulin* at 2 dpf were examined. Transgenic larvae were mounted in 1 %
896 low melt agarose in E3 media containing 0.03 % tricaine and one of the following: 500 nM
897 nocodazole, 25 µM taxol or 0.1 % DMSO (control). Samples were imaged on an inverted Zeiss
898 LSM 780 (Zen 2.3 SP1) confocal microscope with Airyscan, along with a 63x NA 1.4 oil objective
899 lens. Z-stacks encompassing the entire neuromast were acquired every 0.18 µm with an 0.04
900 µm x-y pixel size and Airyscan autoprocessed in 3D.
901 To quantification of ribbon numbers before and after 3-4 hr nocodazole and taxol
902 treatment or in *kif1aa* F0 crispants (Figure 6, Figure 6-S2), the custom-written Fiji macro "Live
903 ribbon counter" described above was used to batch-processed the z-stacks. The red channel
904 (Riba-TagRFP) of each z-stack was thresholded (threshold value = 28) and segmented
905 (watershed). The resulting mask was applied to the original red channel. The number of ribbons
906 was then counted using '3D Objects Counter' (threshold = 1, min size = 0, max size = 183500).
907 The counted objects were merged with the green channel (YFP-tubulin). Each z-stack was
908 visually inspected to make sure the objects counted were within hair cells. The number of
909 ribbons per neuromast was determined and divided by the number of hair cells. The difference
910 in ribbon numbers pre- and post-drug treatment was plotted.
911
912 **Confocal imaging and *in vivo* tracking of ribbons**
913 To visualize ribbon precursor movement, timelapses of double transgenic *myo6b:riba-TagRFP*
914 and *myo6b:YFP-tubulin* larvae at 2 dpf were imaged. For pharmacological treatments,
915 transgenic larvae were mounted in 1 % low melt agarose in E3 media containing 0.03 % tricaine
916 and one of the following: 500 nM nocodazole, 25 µM taxol or 0.1 % DMSO (control) in a glass-
917 bottom dish. Double transgenic *kif1aa* crispants and uninjected controls were mounted in 1 %
918 low melt agarose in E3 media containing 0.03 % tricaine in a glass-bottom dish. Larvae were
919 imaged on an inverted Zeiss LSM 780 or an upright LSM 980 confocal microscope with Airyscan
920 using a 63x 1.4 NA oil objective lens. Airyscan z-stacks of partial cell volumes (~3 µm, 15-20 z-
921 slices using 0.18 µm z-interval and an 0.04 µm x-y pixel size) were taken on the LSM 780 every
922 50-100 s for 30-70 min. Faster LSM 980 Airyscan z-stacks of partial cell volumes (~2-3.5 µm, 12-

923 20 z-slices using 0.17 µm z interval and an 0.04 µm x-y pixel size) were taken every 3-20 s for 5-
924 40 min. Airyscan timelapses were autoprocessed in 3D. In addition, we acquired a subset of
925 LSM 780 Airyscan z-stacks every 5-8 min for 30-100 min to capture fusion events more clearly
926 for Movies S9-11.

927 Timelapses were registered using the FIJI plugin "Correct 3D drift". Drift-corrected
928 timelapses were then tracked in 3D in Imaris using spot detection with estimated xy diameters
929 of 0.427 µm (with background subtraction). The spots were filtered based on 'Quality', with
930 thresholds between 3-8, chosen after visual inspection of the detected spots. For tracking, the
931 'Autoregressive motion' algorithm was used with a maximum linking distance of 1.13 µm and a
932 maximum gap size of 1 frame. Tracks with number of spots < 5 were not included. Using the
933 track displacement length filter in Imaris, the number of tracks with track displacement length >
934 1 µm were counted and divided by the total number of tracks to get the fractions plotted in
935 Figure 3 and 7. Vectors generated in Imaris were used to manually determine the location and
936 direction of tracks with track displacement length > 1 µm. For the mean squared displacement
937 (MSD) analysis, the xyzt coordinates were exported in 'csv' format for all tracks in a timelapse.
938 The MSD analysis was done using the prewritten MATLAB class MSDanalyzer (Tarantino et al.,
939 2014). MSDanalyzer calculates the mean squared displacement for each track, curve-fits the
940 MSD vs time, and provides the value of the exponent (α). The first 25 % of the MSD vs time
941 graph was used for curve-fitting. Tracks with the number of spots < 10 were removed to ensure
942 the accuracy of the MSD analysis. Fusion events between ribbons and precursors were scored
943 manually in these timelapses.

944 **Statistics**

945 All data shown are mean ± standard error of the mean (SEM). All experiments were compiled
946 from data acquired on at least two independent days from different clutches. All replicates
947 were biological–distinct animals and cells. Wild-type animals were selected at random for drug
948 treatments. Datasets were excluded if there was excessive x-y-or z drift. In all datasets dot plots
949 represent the 'n'. N represents either the number of neuromasts, hair cells, synapses, or puncta
950 as stated in the legends. For all zebrafish experiments, a minimum of 3 animals and 6

951 neuromasts were examined. Sample sizes were selected to avoid Type 2 error. All statistical
952 analyses were performed using Prism 10 software (GraphPad). A D'Agostino-Pearson normality
953 test was used to test for normal distributions. To test for statistical significance between two
954 samples, either unpaired t-tests (normally distributed data) or Wilcoxon or Mann-Whitney tests
955 (non-normally distributed data) were used. For multiple comparisons, a one-way ANOVA was
956 used. A P value less than 0.05 was considered significant.

957 **Contributions**

958 KK, SH, and H-TW did the immunohistochemistry, along with the imaging and analysis of fixed
959 samples. KP and MU created the *kif1aa* mutants. KP created *kif1aa* crispants for analyses and
960 made the *myo6b:EB3-GFP* transgenic line. SH did all the live imaging, along with the
961 quantifications and tracking analyses. KK and SH made figures and wrote the manuscript.

962

963 **Data Availability Statement**

964 All data and code used in this paper are available on Dryad: DOI: 10.5061/dryad.crjdfn3gg.

965

966 **Acknowledgements**

967 We thank Drs Juan Angueyra and Katie Drerup for their comments on our manuscript. This
968 work was supported by the National Institute on Deafness and Other Communication Disorders
969 (NIDCD) Intramural Research Program Grant 1ZIADC000085-01 (KK) and Project B08 of the
970 Collaborative Research Center 889 '*Cellular Mechanisms of Sensory Processing*' of the German
971 Research Foundation (MU, awarded to Christian Vogl).

972

973

974 **References**

975 Adamíková L, Straube A, Schulz I, Steinberg G. 2004. Calcium signaling is involved in dynein-
976 dependent microtubule organization. *Mol Biol Cell* **15**:1969–1980.
977 doi:10.1091/mbc.E03-09-0675
978 Ahmari SE, Buchanan J, Smith SJ. 2000. Assembly of presynaptic active zones from cytoplasmic
979 transport packets. *Nat Neurosci* **3**:445–451. doi:10.1038/74814

980 Becker L, Schnee ME, Niwa M, Sun W, Maxeiner S, Talaei S, Kachar B, Rutherford MA, Ricci AJ.
981 2018. The presynaptic ribbon maintains vesicle populations at the hair cell afferent fiber
982 synapse. *eLife* **7**:e30241. doi:10.7554/eLife.30241
983 Bellotti A, Murphy J, Lin L, Petralia R, Wang Y-X, Hoffman D, O'Leary T. 2021. Paradoxical
984 relationships between active transport and global protein distributions in neurons.
985 *Biophys J* **120**:2085–2101. doi:10.1016/j.bpj.2021.02.048
986 Brandt A, Striessnig J, Moser T. 2003. CaV1.3 channels are essential for development and
987 presynaptic activity of cochlear inner hair cells. *J Neurosci* **23**:10832–10840.
988 Bury LAD, Sabo SL. 2011. Coordinated trafficking of synaptic vesicle and active zone proteins
989 prior to synapse formation. *Neural Develop* **6**:24. doi:10.1186/1749-8104-6-24
990 Carrington B, Varshney GK, Burgess SM, Sood R. 2015. CRISPR-STAT: an easy and reliable PCR-
991 based method to evaluate target-specific sgRNA activity. *Nucleic Acids Res* **43**:e157.
992 doi:10.1093/nar/gkv802
993 Ceriani F, Hendry A, Jeng J-Y, Johnson SL, Stephani F, Olt J, Holley MC, Mammano F, Engel J,
994 Kros CJ, Simmons DD, Marcotti W. 2019. Coordinated calcium signalling in cochlear
995 sensory and non-sensory cells refines afferent innervation of outer hair cells. *EMBO J*
996 **38**:e99839. doi:10.15252/embj.201899839
997 Chang B, Heckenlively JR, Bayley PR, Brecha NC, Davisson MT, Hawes NL, Hirano AA, Hurd RE,
998 Ikeda A, Johnson BA, Mccall MA, Morgans CW, Nusinowitz S, Peachey NS, Rice DS,
999 Vessey KA, Gregg RG. 2006. The nob2 mouse, a null mutation in Cacna1f: Anatomical
1000 and functional abnormalities in the outer retina and their consequences on ganglion cell
1001 visual responses. *Vis Neurosci* **23**:11–24. doi:10.1017/S095252380623102X
1002 Chernov KG, Barbet A, Hamon L, Ovchinnikov LP, Curmi PA, Pastré D. 2009. Role of
1003 microtubules in stress granule assembly. *J Biol Chem* **284**:36569–36580.
1004 doi:10.1074/jbc.M109.042879
1005 Cochard A, Safieddine A, Combe P, Benassy M-N, Weil D, Gueroui Z. 2023. Condensate
1006 functionalization with microtubule motors directs their nucleation in space and allows
1007 manipulating RNA localization. *EMBO J* **n/a**:e114106. doi:10.15252/embj.2023114106
1008 Corradi E, Dalla Costa I, Gavoci A, Iyer A, Roccuzzo M, Otto TA, Oliani E, Bridi S, Strohbuecker S,
1009 Santos-Rodriguez G, Valdembri D, Serini G, Abreu-Goodger C, Baudet M. 2020. Axonal
1010 precursor miRNAs hitchhike on endosomes and locally regulate the development of
1011 neural circuits. *EMBO J* **39**:e102513. doi:10.15252/embj.2019102513
1012 David S, Pinter K, Nguyen K-K, Lee DS, Lei Z, Sokolova Y, Sheets L, Kindt KS. 2024. Kif1a and
1013 intact microtubules maintain synaptic-vesicle populations at ribbon synapses in
1014 zebrafish hair cells. *J Physiol*. doi:10.1113/JP286263
1015 Dick O, tom Dieck S, Altrock WD, Ammermüller J, Weiler R, Garner CC, Gundelfinger ED,
1016 Brandstätter JH. 2003. The presynaptic active zone protein bassoon is essential for
1017 photoreceptor ribbon synapse formation in the retina. *Neuron* **37**:775–786.
1018 doi:10.1016/s0896-6273(03)00086-2
1019 Dow E, Siletti K, Hudspeth AJ. 2015. Cellular projections from sensory hair cells form polarity-
1020 specific scaffolds during synaptogenesis. *Genes Dev* **29**:1087–1094.
1021 doi:10.1101/gad.259838.115

1022 Façanha ALO, Appelgren H, Tabish M, Okorokov L, Ekwall K. 2002. The endoplasmic reticulum
1023 cation P-type ATPase Cta4p is required for control of cell shape and microtubule
1024 dynamics. *J Cell Biol* **157**:1029–1039. doi:10.1083/jcb.200111012
1025 Farías GG, Cuitino L, Guo X, Ren X, Jarnik M, Mattera R, Bonifacino JS. 2012. Signal-mediated,
1026 AP-1/clathrin-dependent sorting of transmembrane receptors to the somatodendritic
1027 domain of hippocampal neurons. *Neuron* **75**:810–823.
1028 doi:10.1016/j.neuron.2012.07.007
1029 Fejtova A, Davydova D, Bischof F, Lazarevic V, Altrock WD, Romorini S, Schöne C, Zuschratter W,
1030 Kreutz MR, Garner CC, Ziv NE, Gundelfinger ED. 2009. Dynein light chain regulates
1031 axonal trafficking and synaptic levels of Bassoon. *J Cell Biol* **185**:341–355.
1032 doi:10.1083/jcb.200807155
1033 Frank T, Rutherford MA, Strenzke N, Neef A, Pangršič T, Khimich D, Fejtova A, Gundelfinger ED,
1034 Liberman MC, Harke B, Bryan KE, Lee A, Egner A, Riedel D, Moser T. 2010. Bassoon and
1035 the synaptic ribbon organize Ca^2+ channels and vesicles to add release sites and
1036 promote refilling. *Neuron* **68**:724–738. doi:10.1016/j.neuron.2010.10.027
1037 Frederick CE, Zenisek D. 2023. Ribbon synapses and retinal disease: review. *Int J Mol Sci*
1038 **24**:5090. doi:10.3390/ijms24065090
1039 Freeman W. 1928. The function of the lateral line organs. *Science* **68**:205–205.
1040 doi:10.1126/science.68.1757.205
1041 Fu M, Holzbaur ELF. 2014. Integrated regulation of motor-driven organelle transport by
1042 scaffolding proteins. *Trends Cell Biol* **24**:564–574. doi:10.1016/j.tcb.2014.05.002
1043 Gerdes HH, Rosa P, Phillips E, Baeuerle PA, Frank R, Argos P, Huttner WB. 1989. The primary
1044 structure of human secretogranin II, a widespread tyrosine-sulfated secretory granule
1045 protein that exhibits low pH- and calcium-induced aggregation. *J Biol Chem* **264**:12009–
1046 12015. doi:10.1016/S0021-9258(18)80167-3
1047 Graydon CW, Manor U, Kindt KS. 2017. In vivo ribbon mobility and turnover of Ribeye at
1048 zebrafish hair cell synapses. *Sci Rep* **7**:7467. doi:10.1038/s41598-017-07940-z
1049 Guillet M, Sendin G, Bourien J, Puel J-L, Nouvian R. 2016. Actin filaments regulate exocytosis at
1050 the hair cell ribbon synapse. *J Neurosci* **36**:649–654. doi:10.1523/JNEUROSCI.3379-
1051 15.2016
1052 Gundelfinger ED, Reissner C, Garner CC. 2016. Role of bassoon and piccolo in assembly and
1053 molecular organization of the active zone. *Front Synaptic Neurosci* **7**:19.
1054 doi:10.3389/fnsyn.2015.00019
1055 Gupta RS. 1985. Species-specific differences in toxicity of antimitotic agents toward cultured
1056 mammalian cells2. *JNCI J Natl Cancer Inst* **74**:159–164. doi:10.1093/jnci/74.1.159
1057 Hoshijima K, Jurynec MJ, Klatt Shaw D, Jacobi AM, Behlke MA, Grunwald DJ. 2019. Highly
1058 efficient crispr-cas9-based methods for generating deletion mutations and f0 embryos
1059 that lack gene function in zebrafish. *Dev Cell* **51**:645-657.e4.
1060 doi:10.1016/j.devcel.2019.10.004
1061 Hummel JJA, Hoogenraad CC. 2021. Specific KIF1A-adaptor interactions control selective cargo
1062 recognition. *J Cell Biol* **220**:e202105011. doi:10.1083/jcb.202105011
1063 Janke C, Magiera MM. 2020. The tubulin code and its role in controlling microtubule properties
1064 and functions. *Nat Rev Mol Cell Biol* **21**:307–326. doi:10.1038/s41580-020-0214-3

1065 Jean P, Lopez de la Morena D, Michanski S, Jaime Tobón LM, Chakrabarti R, Picher MM, Neef J,
1066 Jung S, Gültas M, Maxeiner S, Neef A, Wichmann C, Strenzke N, Grabner C, Moser T.
1067 2018. The synaptic ribbon is critical for sound encoding at high rates and with temporal
1068 precision. *eLife* **7**:e29275. doi:10.7554/eLife.29275
1069 Jing Z, Rutherford MA, Takago H, Frank T, Fejtova A, Khimich D, Moser T, Strenzke N. 2013.
1070 Disruption of the presynaptic cytomatrix protein bassoon degrades ribbon anchorage,
1071 multiquantal release, and sound encoding at the hair cell afferent synapse. *J Neurosci*
1072 **33**:4456–67. doi:10.1523/JNEUROSCI.3491-12.2013
1073 Kawano D, Pinter K, Chlebowski M, Petralia RS, Wang Y-X, Nechiporuk AV, Drerup CM. 2022.
1074 NudC regulated Lis1 stability is essential for the maintenance of dynamic microtubule
1075 ends in axon terminals. *iScience* **25**:105072. doi:10.1016/j.isci.2022.105072
1076 Khimich D, Nouvian R, Pujol R, Tom Dieck S, Egner A, Gundelfinger ED, Moser T. 2005. Hair cell
1077 synaptic ribbons are essential for synchronous auditory signalling. *Nature* **434**:889–894.
1078 doi:10.1038/nature03418
1079 Kindt KS, Finch G, Nicolson T. 2012. Kinocilia mediate mechanosensitivity in developing
1080 zebrafish hair cells. *Dev Cell* **23**:329–341. doi:10.1016/j.devcel.2012.05.022
1081 Kujawa SG, Liberman MC. 2015. Synaptopathy in the noise-exposed and aging cochlea: primary
1082 neural degeneration in acquired sensorineural hearing loss. *Hear Res* **330**:191–199.
1083 doi:10.1016/j.heares.2015.02.009
1084 Kwan KM, Fujimoto E, Grabher C, Mangum BD, Hardy ME, Campbell DS, Parant JM, Yost HJ,
1085 Kanki JP, Chien C-B. 2007. The Tol2kit: a multisite gateway-based construction kit for
1086 Tol2 transposon transgenesis constructs. *Dev Dyn Off Publ Am Assoc Anat* **236**:3088–
1087 3099. doi:10.1002/dvdy.21343
1088 Laisne M-C, Michallet S, Lafanechère L. 2021. Characterization of microtubule destabilizing
1089 drugs: a quantitative cell-based assay that bridges the gap between tubulin based- and
1090 cytotoxicity assays. *Cancers* **13**:5226. doi:10.3390/cancers13205226
1091 Leighton AH, Lohmann C. 2016. The wiring of developing sensory circuits-from patterned
1092 spontaneous activity to synaptic plasticity mechanisms. *Front Neural Circuits* **10**:71.
1093 doi:10.3389/fncir.2016.00071
1094 Lepelletier L, de Monvel JB, Buisson J, Desdouets C, Petit C. 2013. Auditory hair cell centrioles
1095 undergo confined brownian motion throughout the developmental migration of the
1096 kinocilium. *Biophys J* **105**:48–58. doi:10.1016/j.bpj.2013.05.009
1097 Luo Y-Y, Wu J-J, Li Y-M. 2021. Regulation of liquid–liquid phase separation with focus on post-
1098 translational modifications. *Chem Commun* **57**:13275–13287. doi:10.1039/D1CC05266G
1099 Lush ME, Diaz DC, Koenecke N, Baek S, Boldt H, St Peter MK, Gaitan-Escudero T, Romero-
1100 Carvajal A, Busch-Nentwich EM, Perera AG, Hall KE, Peak A, Haug JS, Piotrowski T. 2019.
1101 scRNA-Seq reveals distinct stem cell populations that drive hair cell regeneration after
1102 loss of Fgf and Notch signaling. *eLife* **8**:e44431. doi:10.7554/eLife.44431
1103 Lv C, Stewart WJ, Akanyeti O, Frederick C, Zhu J, Santos-Sacchi J, Sheets L, Liao JC, Zenisek D.
1104 2016. Synaptic ribbons require ribeye for electron density, proper synaptic localization,
1105 and recruitment of calcium channels. *Cell Rep* **15**:2784–2795.
1106 doi:10.1016/j.celrep.2016.05.045

1107 Maas C, Torres VI, Altrock WD, Leal-Ortiz S, Wagh D, Terry-Lorenzo RT, Fejtova A, Gundelfinger
1108 ED, Ziv NE, Garner CC. 2012. Formation of Golgi-derived active zone precursor vesicles. *J*
1109 *Neurosci* **32**:11095–11108. doi:10.1523/JNEUROSCI.0195-12.2012
1110 Magupalli VG, Schwarz K, Alpadi K, Natarajan S, Seigel GM, Schmitz F. 2008. Multiple RIBEYE-
1111 RIBEYE interactions create a dynamic scaffold for the formation of synaptic ribbons. *J*
1112 *Neurosci* **28**:7954–7967. doi:10.1523/JNEUROSCI.1964-08.2008
1113 Maxeiner S, Luo F, Tan A, Schmitz F, Südhof TC. 2016. How to make a synaptic ribbon: RIBEYE
1114 deletion abolishes ribbons in retinal synapses and disrupts neurotransmitter release.
1115 *EMBO J* **35**:1098–1114. doi:10.15252/embj.201592701
1116 Merriam EB, Millette M, Lumbard DC, Saengsawang W, Fothergill T, Hu X, Ferhat L, Dent EW.
1117 2013. Synaptic regulation of microtubule dynamics in dendritic spines by calcium, F-
1118 actin, and drebrin. *J Neurosci* **33**:16471–16482. doi:10.1523/JNEUROSCI.0661-13.2013
1119 Michanski S, Kapoor R, Steyer AM, Möbius W, Früholz I, Ackermann F, Gültas M, Garner CC,
1120 Hamra FK, Neef J, Strenzke N, Moser T, Wichmann C. 2023. Piccolino is required for
1121 ribbon architecture at cochlear inner hair cell synapses and for hearing. *EMBO Rep*
1122 **n/a**:e56702. doi:10.15252/embr.202256702
1123 Michanski S, Smaluch K, Steyer AM, Chakrabarti R, Setz C, Oestreicher D, Fischer C, Möbius W,
1124 Moser T, Vogl C, Wichmann C. 2019. Mapping developmental maturation of inner hair
1125 cell ribbon synapses in the apical mouse cochlea. *Proc Natl Acad Sci* **116**:6415–6424.
1126 doi:10.1073/pnas.1812029116
1127 Niwa S, Tanaka Y, Hirokawa N. 2008. KIF1Bβ- and KIF1A-mediated axonal transport of
1128 presynaptic regulator Rab3 occurs in a GTP-dependent manner through DENN/MADD.
1129 *Nat Cell Biol* **10**:1269–1279. doi:10.1038/ncb1785
1130 Obholzer N, Wolfson S, Trapani JG, Mo W, Nechiporuk A, Busch-Nentwich E, Seiler C, Sidi S,
1131 Söllner C, Duncan RN, Boehland A, Nicolson T. 2008. Vesicular glutamate transporter 3 is
1132 required for synaptic transmission in zebrafish hair cells. *J Neurosci* **28**:2110–2118.
1133 doi:10.1523/JNEUROSCI.5230-07.2008
1134 Ohta S, Ji YR, Martin D, Wu DK. 2020. Emx2 regulates hair cell rearrangement but not positional
1135 identity within neuromasts. *eLife*. doi:10.7554/eLife.60432
1136 Okada Y, Yamazaki H, Sekine-Aizawa Y, Hirokawa N. 1995. The neuron-specific kinesin
1137 superfamily protein KIF1A is a unique monomeric motor for anterograde axonal
1138 transport of synaptic vesicle precursors. *Cell* **81**:769–780. doi:10.1016/0092-
1139 8674(95)90538-3
1140 Oliver D, Ramachandran S, Philbrook A, Lambert CM, Nguyen KCQ, Hall DH, Francis MM. 2022.
1141 Kinesin-3 mediated axonal delivery of presynaptic neurexin stabilizes dendritic spines
1142 and postsynaptic components. *PLoS Genet* **18**:e1010016.
1143 doi:10.1371/journal.pgen.1010016
1144 Pack-Chung E, Kurshan PT, Dickman DK, Schwarz TL. 2007. A Drosophila kinesin required for
1145 synaptic bouton formation and synaptic vesicle transport. *Nat Neurosci* **10**:980–989.
1146 doi:10.1038/nn1936
1147 Parslow A, Cardona A, Bryson-Richardson RJ. 2014. Sample drift correction following 4D
1148 confocal time-lapse imaging. *J Vis Exp JoVE* 51086. doi:10.3791/51086

1149 Regus-Leidig H, Fuchs M, Löhner M, Leist SR, Leal-Ortiz S, Chiodo VA, Hauswirth WW, Garner
1150 CC, Brandstätter JH. 2014. In vivo knockdown of Piccolino disrupts presynaptic ribbon
1151 morphology in mouse photoreceptor synapses. *Front Cell Neurosci* **8**.
1152 Regus-Leidig H, tom Dieck S, Specht D, Meyer L, Brandstätter JH. 2009. Early steps in the
1153 assembly of photoreceptor ribbon synapses in the mouse retina: The involvement of
1154 precursor spheres. *J Comp Neurol* **512**:814–824. doi:10.1002/cne.21915
1155 Roux I, Hosie S, Johnson SL, Bahloul A, Cayet N, Nouaille S, Kros CJ, Petit C, Safieddine S. 2009.
1156 Myosin VI is required for the proper maturation and function of inner hair cell ribbon
1157 synapses. *Hum Mol Genet* **18**:4615–4628. doi:10.1093/hmg/ddp429
1158 Ruel J, Emery S, Nouvian R, Bersot T, Amilhon B, Van Rybroek JM, Rebillard G, Lenoir M, Eybalin
1159 M, Delprat B, Sivakumaran TA, Giros B, El Mestikawy S, Moser T, Smith RJH, Lesperance
1160 MM, Puel J-L. 2008. Impairment of SLC17A8 encoding vesicular glutamate transporter-3,
1161 VGLUT3, underlies nonsyndromic deafness DFNA25 and inner hair cell dysfunction in
1162 null mice. *Am J Hum Genet* **83**:278–292. doi:10.1016/j.ajhg.2008.07.008
1163 Sampo B, Kaech S, Kunz S, Banker G. 2003. Two distinct mechanisms target membrane proteins
1164 to the axonal surface. *Neuron* **37**:611–624. doi:10.1016/s0896-6273(03)00058-8
1165 Schmitz F. 2009. The making of synaptic ribbons: how they are built and what they do. *Neurosci*
1166 *Rev J Bringing Neurobiol Neurol Psychiatry* **15**:611–624.
1167 doi:10.1177/1073858409340253
1168 Schmitz F, Königstorfer A, Südhof TC. 2000. RIBEYE, a component of synaptic ribbons: a
1169 protein's journey through evolution provides insight into synaptic ribbon function.
1170 *Neuron* **28**:857–872. doi:10.1016/S0896-6273(00)00159-8
1171 Schrøder JM, Larsen J, Komarova Y, Akhmanova A, Thorsteinsson RI, Grigoriev I, Manguso R,
1172 Christensen ST, Pedersen SF, Geimer S, Pedersen LB. 2011. EB1 and EB3 promote cilia
1173 biogenesis by several centrosome-related mechanisms. *J Cell Sci* **124**:2539–2551.
1174 doi:10.1242/jcs.085852
1175 Shapira M, Zhai RG, Dresbach T, Bresler T, Torres VI, Gundelfinger ED, Ziv NE, Garner CC. 2003.
1176 Unitary assembly of presynaptic active zones from Piccolo-Bassoon transport vesicles.
1177 *Neuron* **38**:237–252. doi:10.1016/s0896-6273(03)00207-1
1178 Sheets L, Holmgren M, Kindt KS. 2021. How zebrafish can drive the future of genetic-based
1179 hearing and balance research. *JARO J Assoc Res Otolaryngol* **22**:215–235.
1180 doi:10.1007/s10162-021-00798-z
1181 Sheets L, Kindt KS, Nicolson T. 2012. Presynaptic CaV1.3 channels regulate synaptic ribbon size
1182 and are required for synaptic maintenance in sensory hair cells. *J Neurosci* **32**:17273–
1183 17286. doi:10.1523/JNEUROSCI.3005-12.2012
1184 Sheets L, Trapani JG, Mo W, Obholzer N, Nicolson T. 2011. Ribeye is required for presynaptic
1185 Ca(V)1.3a channel localization and afferent innervation of sensory hair cells. *Dev Camb*
1186 *Engl* **138**:1309–1319. doi:10.1242/dev.059451
1187 Sikora G, Teuerle M, Wyłomańska A, Grebenkov D. 2017. Statistical properties of the
1188 anomalous scaling exponent estimator based on time-averaged mean-square
1189 displacement. *Phys Rev E* **96**:022132. doi:10.1103/PhysRevE.96.022132
1190 Sobkowicz HM, Rose JE, Scott GE, Slapnick SM. 1982. Ribbon synapses in the developing intact
1191 and cultured organ of Corti in the mouse. *J Neurosci* **2**:942–957.
1192 doi:10.1523/JNEUROSCI.02-07-00942.1982

1193 Sobkowicz HM, Rose JE, Scott GL, Levenick CV. 1986. Distribution of synaptic ribbons in the
1194 developing organ of Corti. *J Neurocytol* **15**:693–714. doi:10.1007/BF01625188
1195 Stepanova T, Slemmer J, Hoogenraad CC, Lansbergen G, Dortland B, Zeeuw CID, Grosveld F,
1196 Cappellen G van, Akhmanova A, Galjart N. 2003. Visualization of microtubule growth in
1197 cultured neurons via the use of eb3-gfp (end-binding protein 3-green fluorescent
1198 protein). *J Neurosci* **23**:2655–2664. doi:10.1523/JNEUROSCI.23-07-02655.2003
1199 Suli A, Watson GM, Rubel EW, Raible DW. 2012. Rheotaxis in larval zebrafish is mediated by
1200 lateral line mechanosensory hair cells. *PLoS ONE* **7**. doi:10.1371/journal.pone.0029727
1201 Sur A, Wang Y, Capar P, Margolin G, Prochaska MK, Farrell JA. 2023. Single-cell analysis of
1202 shared signatures and transcriptional diversity during zebrafish development. *Dev Cell*
1203 **58**:3028-3047.e12. doi:10.1016/j.devcel.2023.11.001
1204 Sweeney HL, Holzbaur ELF. 2018. Motor Proteins. *Cold Spring Harb Perspect Biol* **10**:a021931.
1205 doi:10.1101/cshperspect.a021931
1206 Tarantino N, Tinevez J-Y, Crowell EF, Boisson B, Henriques R, Mhlanga M, Agou F, Israël A,
1207 Laplantine E. 2014. TNF and IL-1 exhibit distinct ubiquitin requirements for inducing
1208 NEMO–IKK supramolecular structures. *J Cell Biol* **204**:231–245.
1209 doi:10.1083/jcb.201307172
1210 Tinevez J-Y, Perry N, Schindelin J, Hoopes GM, Reynolds GD, Laplantine E, Bednarek SY, Shorte
1211 SL, Eliceiri KW. 2017. TrackMate: An open and extensible platform for single-particle
1212 tracking. *Methods*, Image Processing for Biologists **115**:80–90.
1213 doi:10.1016/j.ymeth.2016.09.016
1214 Trapani JG, Obholzer N, Mo W, Brockerhoff SE, Nicolson T. 2009. Synaptojanin1 is required for
1215 temporal fidelity of synaptic transmission in hair cells. *PLOS Genet* **5**:e1000480.
1216 doi:10.1371/journal.pgen.1000480
1217 Tritsch NX, Yi E, Gale JE, Glowatzki E, Bergles DE. 2007. The origin of spontaneous activity in the
1218 developing auditory system. *Nature* **450**:50–55. doi:10.1038/nature06233
1219 Uthaiah RC, Hudspeth AJ. 2010. Molecular anatomy of the hair cell's ribbon synapse. *J Neurosci*
1220 **30**:12387–12399. doi:10.1523/JNEUROSCI.1014-10.2010
1221 Varshney GK, Carrington B, Pei W, Bishop K, Chen Z, Fan C, Xu L, Jones M, LaFave MC, Ledin J,
1222 Sood R, Burgess SM. 2016. A high-throughput functional genomics workflow based on
1223 CRISPR/Cas9-mediated targeted mutagenesis in zebrafish. *Nat Protoc* **11**:2357–2375.
1224 doi:10.1038/nprot.2016.141
1225 Vleugel M, Kok M, Dogterom M. 2016. Understanding force-generating microtubule systems
1226 through in vitro reconstitution. *Cell Adhes Migr* **10**:475–494.
1227 doi:10.1080/19336918.2016.1241923
1228 Voorn RA, Sternbach M, Jarysta A, Rankovic V, Tarchini B, Wolf F, Vogl C. 2024. Slow kinesin-
1229 dependent microtubular transport facilitates ribbon synapse assembly in developing
1230 cochlear inner hair cells. *eLife* **13**. doi:10.7554/eLife.98145.1
1231 Wan G, Ji L, Schrepfer T, Gong S, Wang G-P, Corfas G. 2019. Synaptopathy as a mechanism for
1232 age-related vestibular dysfunction in mice. *Front Aging Neurosci* **11**:156.
1233 doi:10.3389/fnagi.2019.00156
1234 Wang B, Zhang Lei, Dai T, Qin Z, Lu H, Zhang Long, Zhou F. 2021. Liquid–liquid phase separation
1235 in human health and diseases. *Signal Transduct Target Ther* **6**:1–16.
1236 doi:10.1038/s41392-021-00678-1

1237 Wang Z, Lou J, Zhang H. 2022. Essence determines phenomenon: Assaying the material
1238 properties of biological condensates. *J Biol Chem* **298**. doi:10.1016/j.jbc.2022.101782
1239 Wiegand T, Hyman AA. 2020. Drops and fibers — how biomolecular condensates and
1240 cytoskeletal filaments influence each other. *Emerg Top Life Sci* **4**:247–261.
1241 doi:10.1042/ETLS20190174
1242 Wong HC, Zhang Q, Beirl AJ, Petralia RS, Wang Y-X, Kindt K. 2019. Synaptic mitochondria
1243 regulate hair-cell synapse size and function. *eLife* **8**:e48914. doi:10.7554/eLife.48914
1244 Yamada M, Tanaka-Takiguchi Y, Hayashi M, Nishina M, Goshima G. 2017. Multiple kinesin-14
1245 family members drive microtubule minus end–directed transport in plant cells. *J Cell Biol*
1246 **216**:1705–1714. doi:10.1083/jcb.201610065
1247 Yoo SH. 1995. Ph- and ca2+-induced conformational change and aggregation of chromogranin
1248 b.: comparison with chromogranin a and implication in secretory vesicle biogenesis (*). *J*
1249 *Biol Chem* **270**:12578–12583. doi:10.1074/jbc.270.21.12578
1250 Zhang Q, Kindt KS. 2022. Using light-sheet microscopy to study spontaneous activity in the
1251 developing lateral-line system. *Front Cell Dev Biol* **10**:819612.
1252 doi:10.3389/fcell.2022.819612
1253 Zieve GW, Turnbull D, Mullins JM, McIntosh JR. 1980. Production of large numbers of mitotic
1254 mammalian cells by use of the reversible microtubule inhibitor nocodazole. Nocodazole
1255 accumulated mitotic cells. *Exp Cell Res* **126**:397–405. doi:10.1016/0014-4827(80)90279-
1256 7
1257
1258
1259
1260
1261
1262
1263
1264
1265
1266
1267
1268
1269
1270
1271
1272

1273 **Figures and Legends**

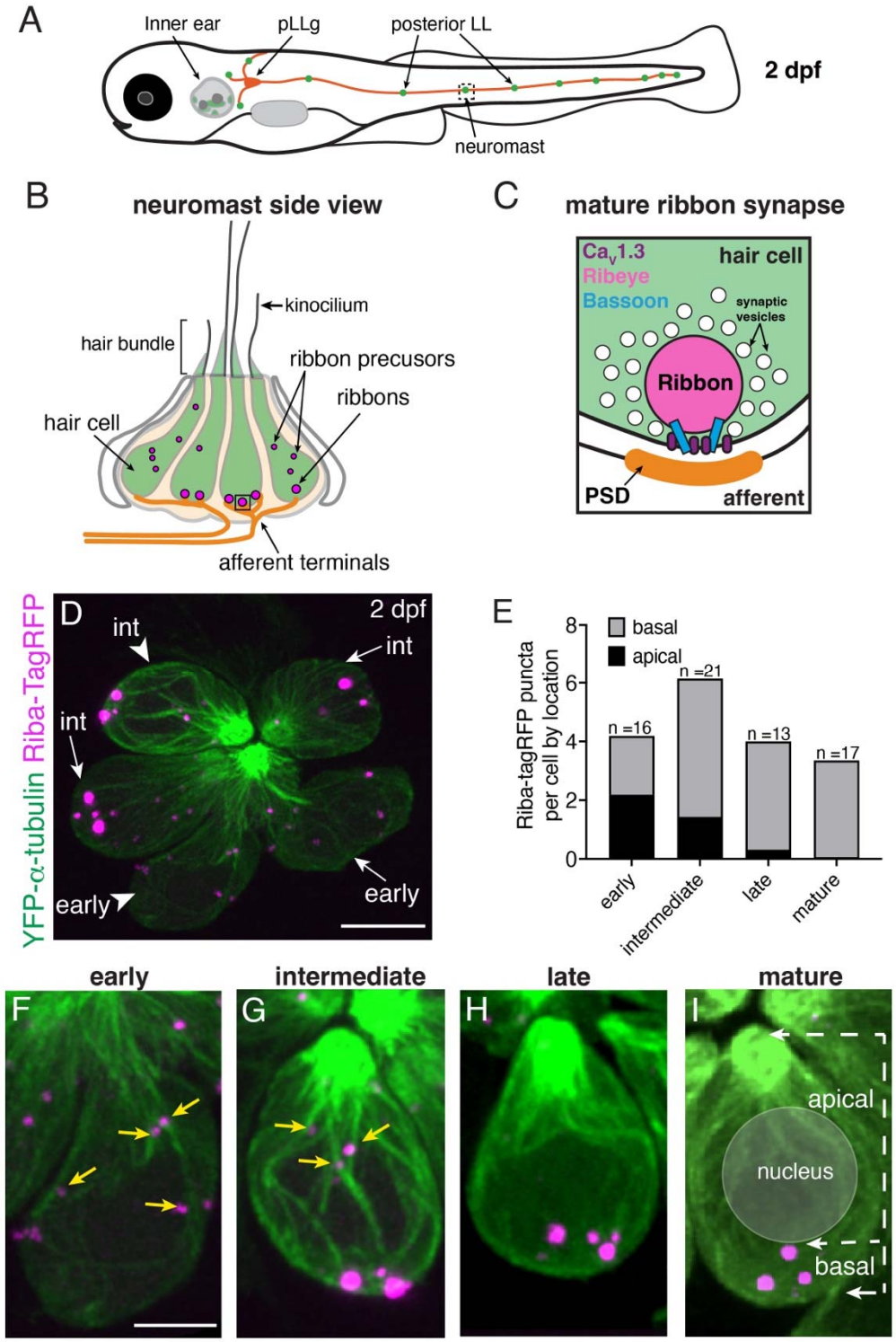

1274

1275 **Figure 1 – Ribbons associate with microtubules and change localization during development**

1276 **A)** Schematic of a larval zebrafish at 2 days post fertilization (dpf) with the location of the

1277 posterior-lateral line (pLL) indicated relative to the inner ear. Neuromasts (green) in the

1278 posterior LL contain sensory hair cells that are innervated by afferent projections from the
1279 posterior LL ganglion (pLLg, orange). **B)** Schematic of a neuromast at 2 dpf, viewed from the
1280 side. At 2 dpf, the majority of hair cells (green) are developing. At the top of the cells, the
1281 mechanosensory hair bundle is composed of actin-based stereocilia and a tubulin-based
1282 kinocilium. A shorter kinocilium and an abundance of small ribbon precursors are indicative of
1283 an immature stage. **C)** Schematic of a ribbon synapse when mature. The dense presynapse or
1284 ribbon is made primarily of Ribeye. Ribbons tether synaptic vesicles near $Ca_V1.3$ channels at the
1285 plasma membrane, across from the postsynaptic density (PSD). Bassoon acts to anchor ribbons
1286 at the presynaptic AZ. **D)** Example image of a neuromast at 2 dpf, viewed from top down. The
1287 microtubule network and ribbons are marked with YFP-Tubulin and Riba-TagRFP respectively. In
1288 this example of 6 developing hair cells, 2 early and 4 intermediate cells are present. The cell
1289 bodies of an early and intermediate cell from this example (arrowheads) are expanded in **F** and
1290 **G**. **E)** Plot shows the average number of ribbons per hair cell at each developmental stage. Cell
1291 stage is determined by the height of the kinocilium. After an increase in ribbon number with
1292 development, there is a decrease upon maturation. The number of apically-localized Riba-
1293 TagRFP puncta is high at early and intermediate stages and is lower in late and mature hair
1294 cells. In contrast, the number of basally-localized Riba-TagRFP puncta is low at early stages and
1295 becomes higher by intermediate stages (n = 16, 21, 13, 17 hair cells for early, intermediate, late,
1296 and mature stages respectively). **F-I)** Example images of hair cells expressing YFP-Tubulin and
1297 Riba-TagRFP at early, intermediate, late, and mature stages. At the early stage, Riba-TagRFP
1298 puncta are spread throughout the cell body and are smaller in size. At the intermediate stage,
1299 the number of Riba-TagRFP puncta becomes more basally enriched and are larger in size. In late
1300 and mature hair cells, all Riba-TagRFP puncta are at the base of the cell and are fewer in
1301 number compared to the intermediate stage. The arrows in **I** highlight the apical and basal
1302 region of the cell used for quantification of Riba-TagRFP puncta location in **E**. Yellow arrows in **E**
1303 and **F** indicate precursors associated with microtubules. Scale bars in **D** = 5 µm and in **F** = 2 µm.
1304

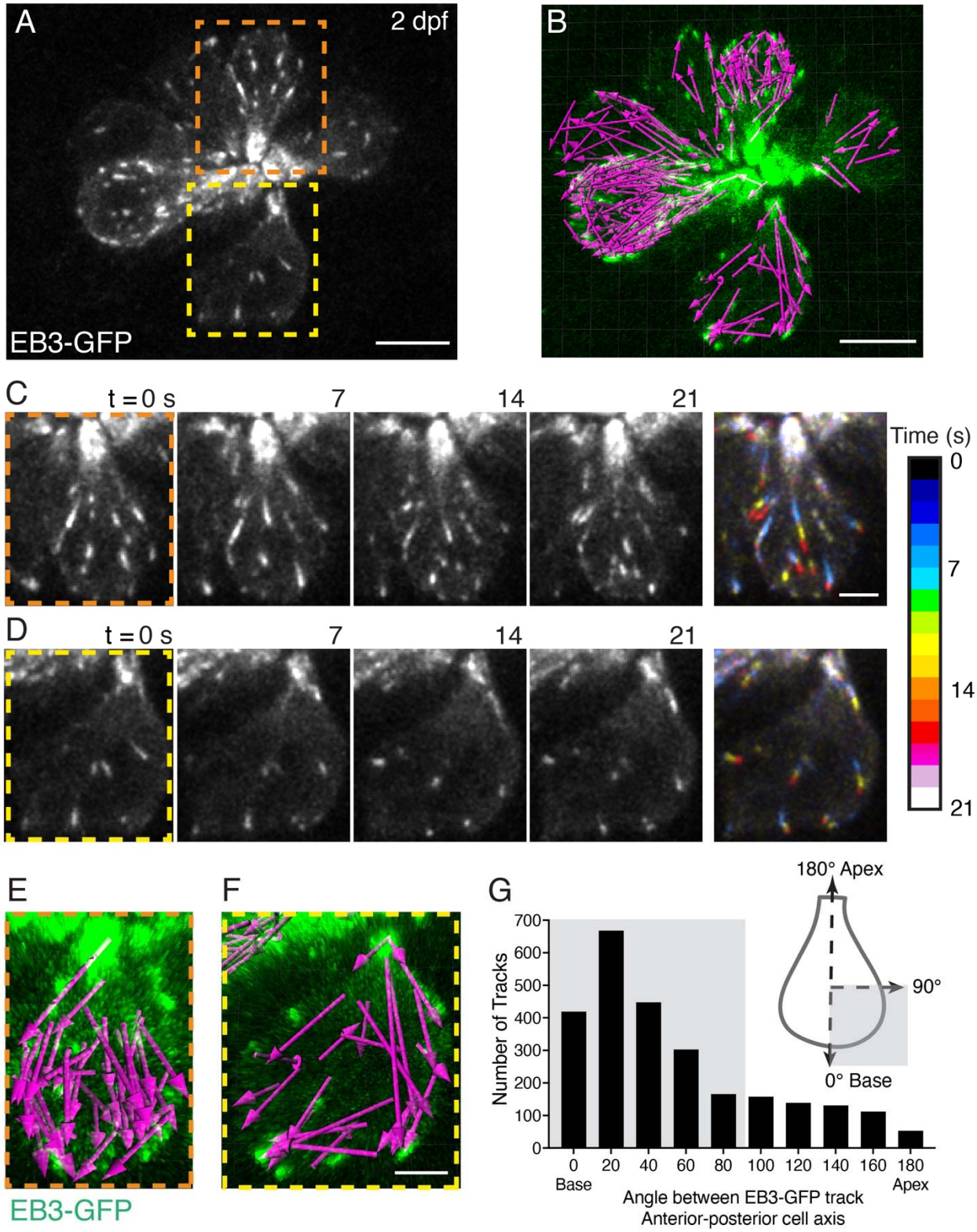

Figure 2 – EB3-GFP tracks show plus ends of microtubules move to the cell base

1307 **A)** Example image of a neuromast at 2 dpf. The growing or plus ends of microtubules are
1308 marked with EB3-GFP. In this example, the apex of 8 developing cells is at the center of the
1309 image and the base of each cell is at the periphery. 2 example cells are outlined (dashed lines)
1310 and expanded in more detail in in **C-D,** and **E-F**. **B)** A 22-min timelapse was taken of the example
1311 in **A**. All EB3-tracks, indicated by magenta arrows (tracked in Imaris) detected during the
1312 timelapse are shown. **C-D)** Example time courses of EB3-GFP in hair cells over 21 s; the cell apex
1313 is towards the top of each image. In the final image, the 4 images for each example (0-21 s)
1314 were projected over time as a pseudocolor image represented by the colormap. The
1315 pseudocolor images show that many EB3-GFP tracks move to the cell base. **E-F)** The magenta
1316 arrows in **E** and **F** show all the EB3-GFP tracks acquired in the example cells in **C-D** over the
1317 entire 22-min duration. Arrowheads indicate the direction of travel. **G)** The schematic in **G**
1318 shows how EB3-GFP tracks were aligned to each hair cell. Tracks moving toward the apex have
1319 a track angle of 180°, while those moving to the base have an angle of 0°. This analysis revealed
1320 that the majority of EB3-GFP tracks (shaded domains) move toward the base of the cell (n = 7
1321 neuromasts, 2597 tracks). Scale bars in **A-B** = 5 µm and in **C-F** = 2 µm.
1322

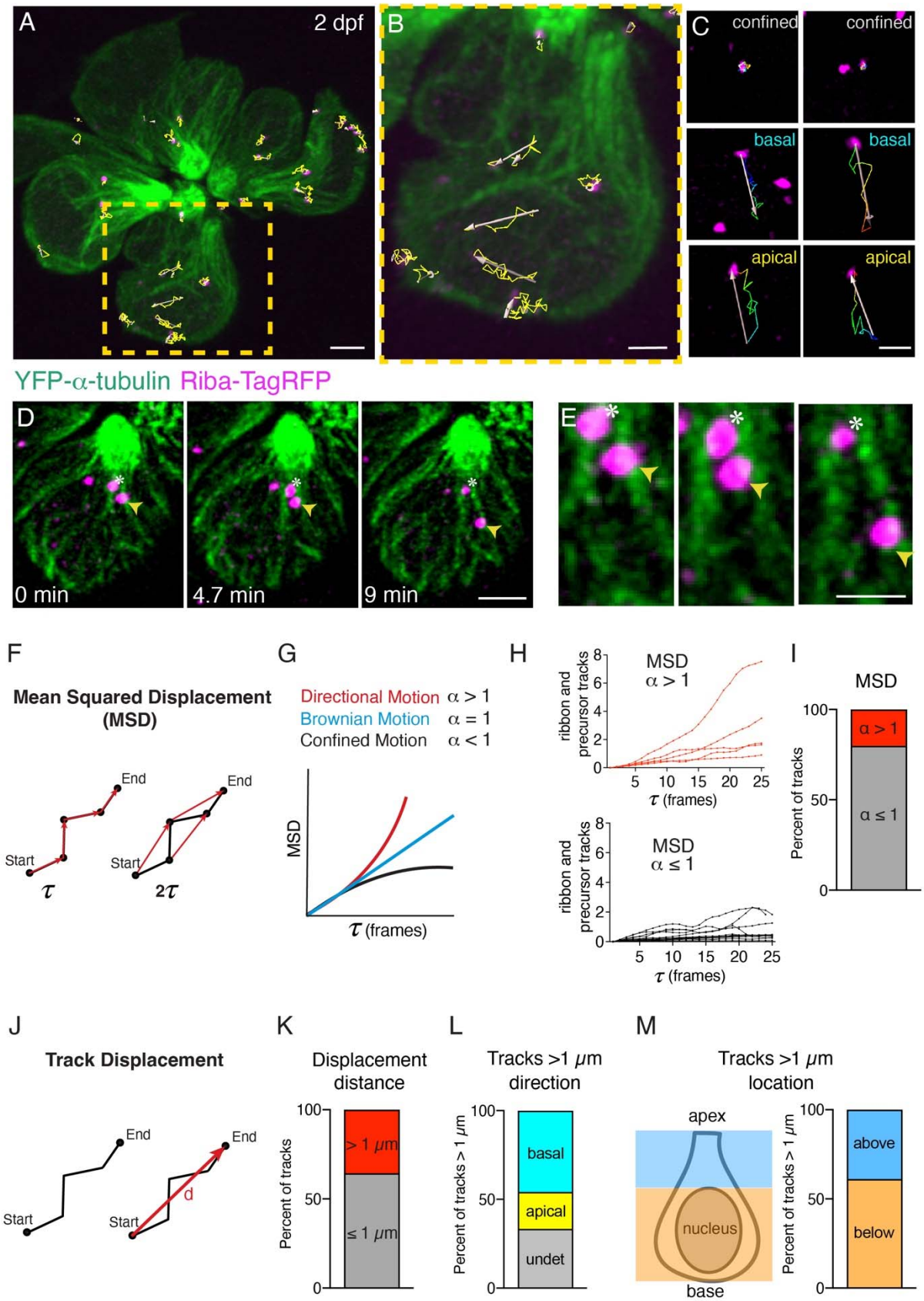
A
2 dpf
B
C
confined
confined
basal
basal
apical
apical
YFP-α-tubulin Riba-TagRFP
D
0 min
4.7 min
9 min
E
F
Mean Squared Displacement (MSD)
End
Start
τ
2τ
G
Directional Motion α > 1
Brownian Motion α = 1
Confined Motion α < 1
MSD
τ (frames)
H
MSD α > 1
MSD α ≤ 1
ribbon and precursor tracks
τ (frames)
I
MSD
Percent of tracks
α > 1
α ≤ 1
J
Track Displacement
d
K
Displacement distance
Percent of tracks
> 1 μm
≤ 1 μm
L
Tracks >1 μm direction
Percent of tracks > 1 μm
basal
apical
undet
M
Tracks >1 μm location
apex
nucleus
base
above
below

1323

1324 **Figure 3 – Ribbon precursors exhibit directional motion and confinement on microtubules**
1325 **A-B)** To quantify motion, ribbons and ribbon precursors were tracked in hair cells at early and
1326 intermediate stages at 2 dpf (example). Shown are tracks (in yellow) from an entire neuromast
1327 (**A**) and a single hair cell (**B**), obtained using Imaris, during a 30-min timelapse acquired every 50
1328 s (also see Movie S2). **C)** Magnified view shows individual tracks over time and examples of
1329 confinement and motion towards the cell base and apex. **D)** Example of confined motion and
1330 directed motion on microtubules in a single hair cell. Movie was obtained during a 9 min
1331 timelapse acquired every 20 s. The ribbon labeled by the asterisks remains confined, while the
1332 ribbon labeled with the yellow arrow moves along a microtubule, towards the cell base, over
1333 time (also see Movie S4). **E)** A magnified image of the example shown in **D. F)** Mean squared
1334 displacement (MSD) vs time step was used to measure movement behaviors. Shown in red are
1335 the first- and second-time steps. The results are plotted in the form of MSD vs time step (τ)
1336 plots and the exponent (α) of the plots can be used to distinguish between the different types
1337 of motion observed (confined ($\alpha < 1$), directional ($\alpha > 1$), or Brownian motion ($\alpha = 1$)). **H)**
1338 Example MSD plots of individual ribbon tracks from 2 control neuromasts (15 tracks MSD < 1
1339 (black), 5 tracks MSD > 1 (red)). **I)** The bar graph shows the percent of MSD tracks displaying
1340 confined ($\alpha < 1$, 79.8 %, gray), and directional motion ($\alpha > 1$, 20.2 %, red). **J)** Track displacement
1341 vs time was used to measure movement behaviors with track > 1 µm indicative of directed
1342 motion. **K)** The bar graph shows the percent of tracks with distances > 1 µm (35.6 % red) and
1343 those with distances ≤ 1 µm (65.4 %, gray). **L)** The bar graph shows the percent of tracks with
1344 distances > 1 µm based on track direction (20.8 % to the cell apex, yellow; 45.8 % to the cell
1345 base, cyan; 33.3 % undetermined direction, gray). **M)** The bar graph shows the percent of tracks
1346 with distances > 1 µm based on location in the cell, above or below the nucleus (38.9 % above
1347 the nucleus, blue; 61.1 % below the nucleus, orange). In **K-M** n = 10 neuromasts, 40 hair cells,
1348 and 203 tracks. Scale bar in **A,D** = 2 µm and **B,C,E** = 1 µm.
1349

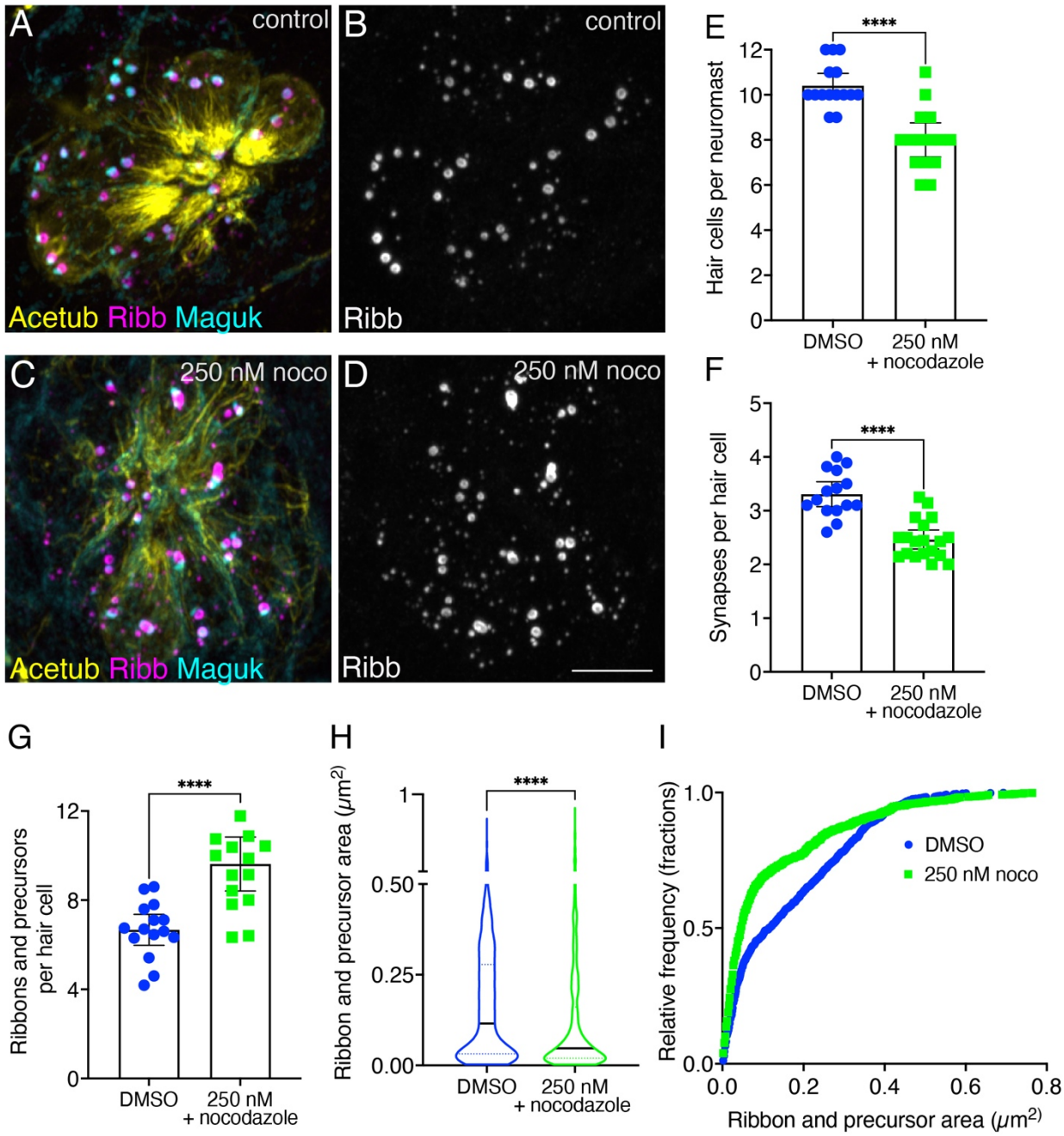

Figure 4 – Overnight microtubule destabilization increases ribbon numbers, and decreases synapse counts and ribbon areas

A-D) Example immunostain of a neuromast at 3 dpf after an overnight treatment with 250 nM nocodazole (**C-D**) or DMSO (**A-B**). Acetylated-α-tubulin (Acetub) labels microtubules, Ribeyeb (Ribb) labels precursors and ribbons, and Maguk labels postsynapses. **E-G**) After an overnight treatment with 250 nM nocodazole there are significantly fewer hair cells per neuromast (**E**, P <

1357 0.0001), fewer complete synapses per cell (**F**, $P < 0.0001$), and more ribbons and precursors per
1358 cell (**G**, $P < 0.0001$) compared to controls (n = 15 neuromasts for control and 250 nM
1359 nocodazole treatments). **H-I**) After an overnight treatment with 250 nM nocodazole the
1360 average area of Ribeyeb puncta was significantly lower compared to controls (**H**, $P < 0.0001$, n =
1361 1008 and 1135 Ribeyeb puncta for control and 250 nM nocodazole treatments). In **I**, the
1362 relative frequency of all the areas of Ribeyeb puncta are plotted in nocodazole treatment and
1363 controls. For comparisons an unpaired t-test was used in **E-G**, and a Mann-Whitney test was
1364 used in **H**. Scale bar in **D** = 5 µm.
1365
1366
1367
1368

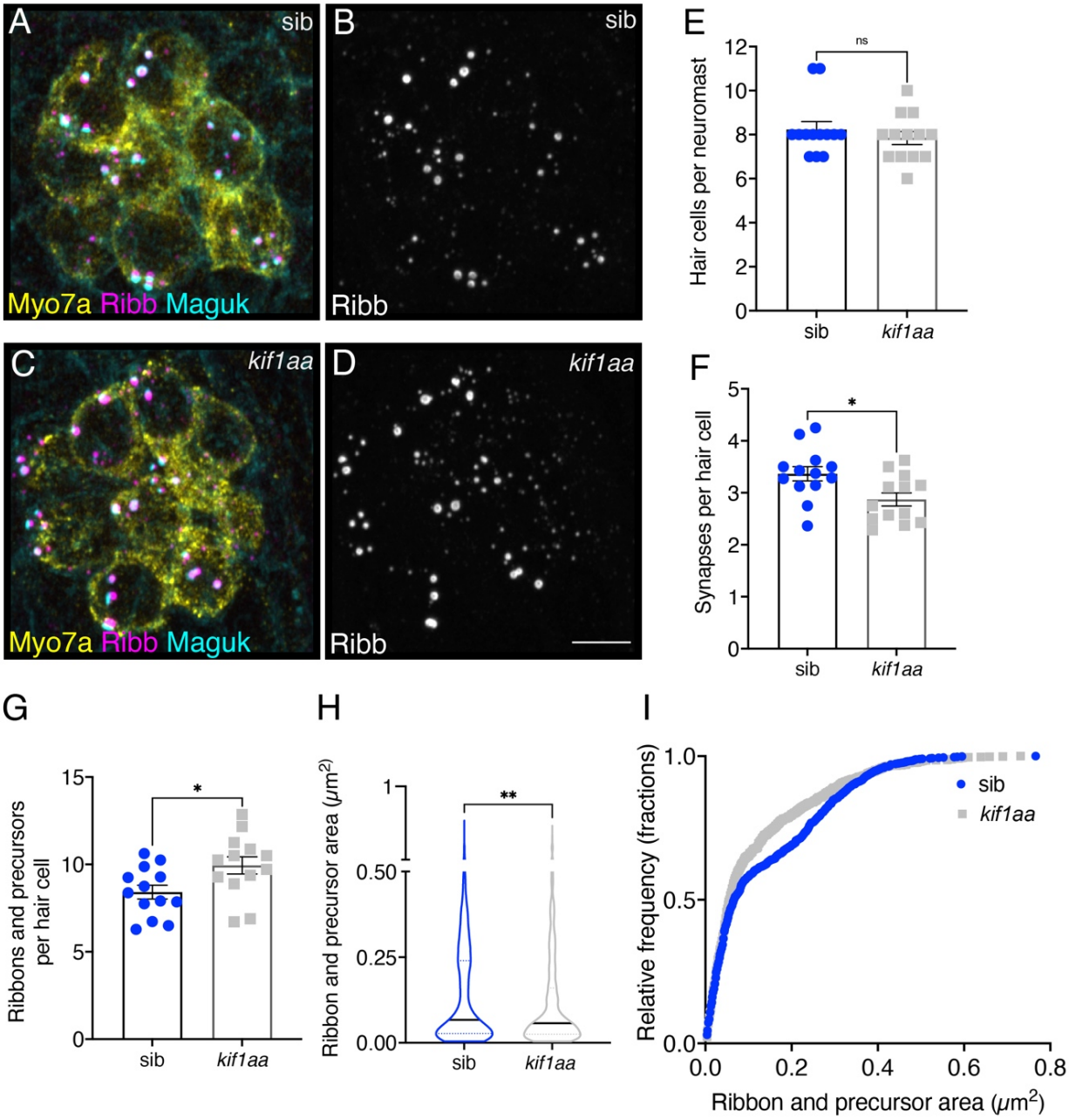

Figure 5 – Loss of Kif1aa increases precursor numbers and decreases synapse counts

A-D) Example immunostain of neuromasts at 3 dpf in *kif1aa* germline mutants (**C-D**) or sibling control (**A-B**). Myosin7a labels hair cells, Ribeyeb (Ribb) labels precursors and ribbons, and Maguk labels postsynapses. **E-G**) In *kif1aa* mutants there is no change in the number of hair cells per neuromast (**E**, P = 0.418), but there are fewer complete synapses per cell (**F**, P = 0.014), and more ribbons and precursors per cell (**G**, P = 0.024) compared to sibling controls (n = 13 neuromasts for control and *kif1aa* mutants). **H-I**) In *kif1aa* germline mutants the average area

1377 of Ribeyeb puncta was significantly lower compared to sibling controls (**H**, P = 0.005, n = 896
1378 and 1008 Ribeyeb puncta for control and *kif1aa* mutants). In **I**, the relative frequency of all the
1379 areas of Ribeyeb puncta are plotted in *kif1aa* mutants and sibling controls. For comparisons an
1380 unpaired t-test was used in **E-G**, and a Mann-Whitney test was used in **H**. Scale bar in **D** = 5 µm.
1381
1382
1383
1384
1385
1386
1387
1388
1389

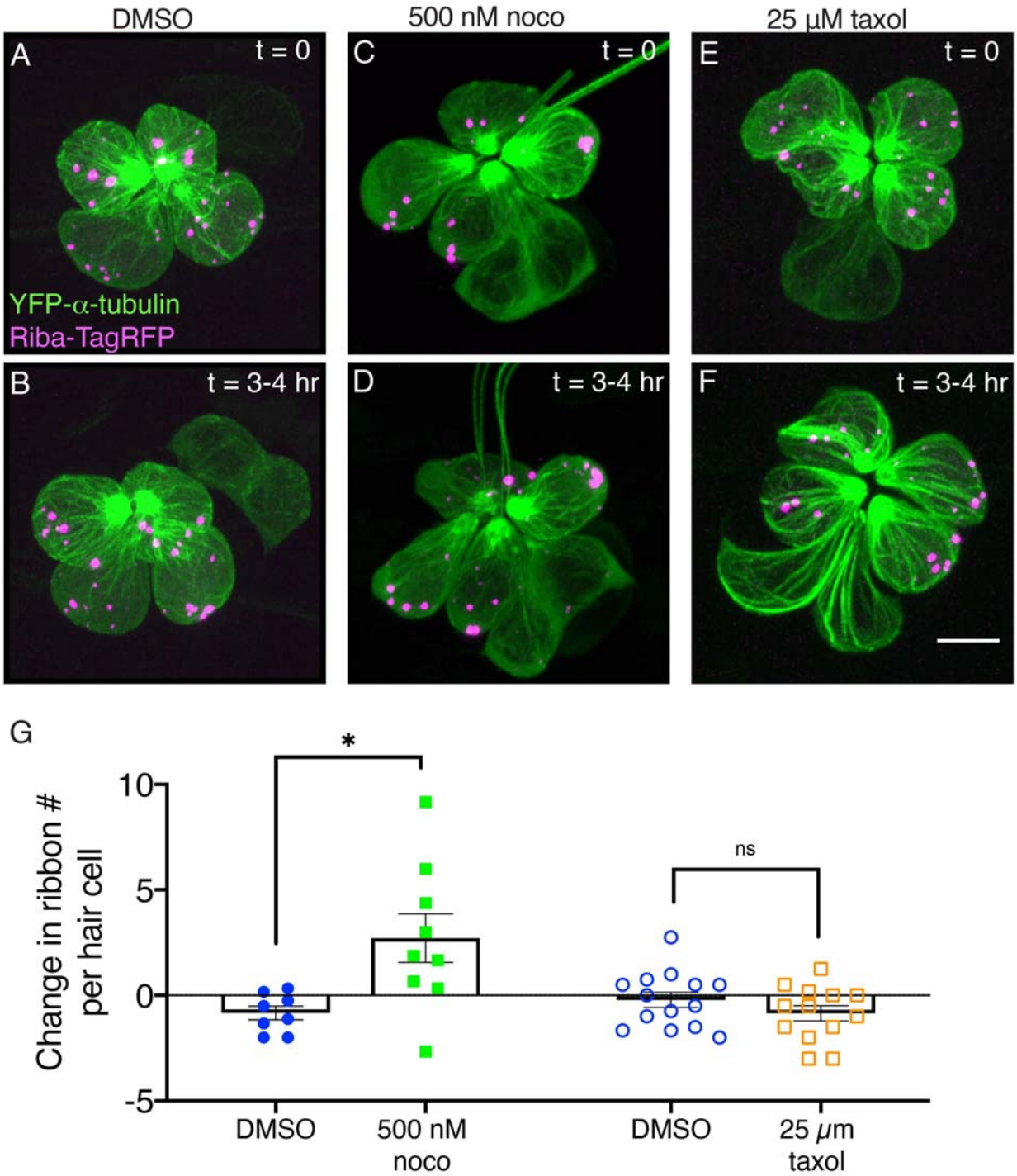

Figure 6 – Microtubule destabilization increases ribbon numbers *in vivo*

A,C,E) Example images of neuromasts at 2 dpf. The microtubule network and ribbons are marked with YFP-tubulin and Riba-TagRFP respectively. Neuromasts were imaged immediately after a 30-min treatment with DMSO (**A**, control) 500 nM nocodazole (**C**) or 25 µM taxol (**E**), (t =

1395 0). **B,D,F**) The same neuromasts in **A,C,E** were reimaged after an additional 3-4 hrs of
1396 treatment. **G**) Quantification reveals that after 3-4 hr nocodazole treatment, there are more
1397 Riba-TagRFP puncta per hair cell compared to controls (n = 9 and 8 neuromasts for nocodazole
1398 and DMSO, P = 0.013). In contrast, after a 3-4 hr taxol treatment, there was no significant
1399 change in the number of Riba-TagRFP puncta per hair cell compared to controls (n = 13 and 14
1400 neuromasts for taxol and DMSO, P = 0.256). An unpaired t-test was used for comparisons in **G**.
1401 Scale bar in **F** = 5 µm.
1402
1403
1404
1405
1406
1407
1408
1409

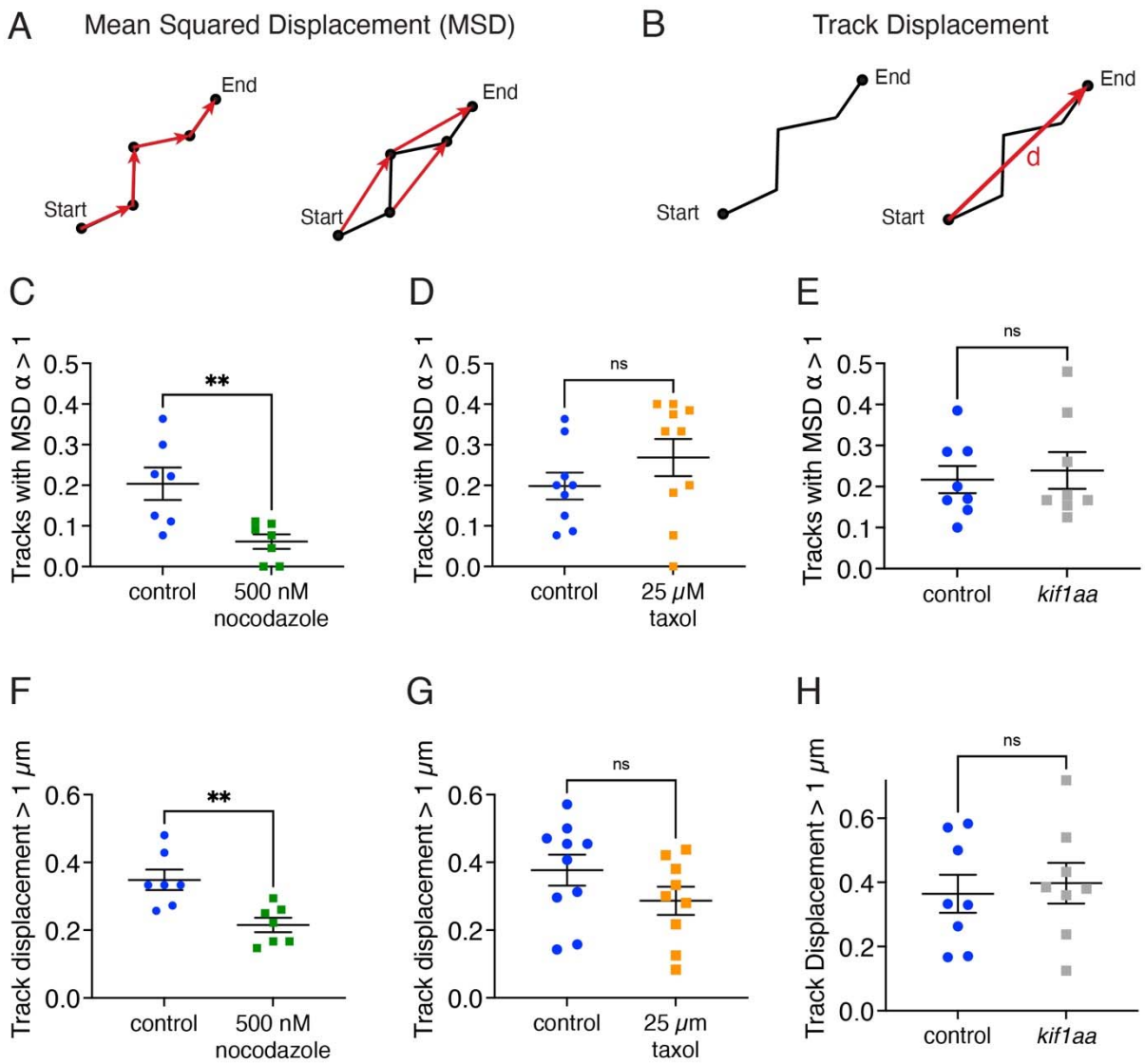

Figure 7 – Ribbon precursors require intact microtubules, but not Kif1aa for directional motion

A) Mean squared displacement (MSD) vs time was used to quantify the proportion of ribbon and precursor tracks with a velocity have $\alpha > 1$, a behavior indicative of directionally moving tracks. Shown are the first- and second-time steps. **B)** To further quantify directional motion, the proportion of tracks with large displacements >1 µm was quantified. Track displacement was measured as the distance between the start and end point of the track. **C)** Hair cells treated

1420 with 500 mM nocodazole have fewer directional tracks ($\alpha > 1$) compared to controls (P =
1421 0.007). **D)** In hair cells treated with 25 µM taxol there are not significantly fewer directional
1422 tracks ($\alpha > 1$) compared to controls (P = 0.24). **E)** In hair cells lacking Kif1aa, there are not
1423 significantly fewer directional tracks ($\alpha > 1$) compared to controls (P =0.70). **F)** Hairs cells
1424 treated with 500 nM nocodazole have fewer ribbons with track displacements > 1 µm
1425 compared to control (P = 0.004). **G)** There is no change in track displacement > 1 µm in hair cells
1426 treated with 25 µM taxol (P = 0.17). **H)** There is no change in track displacement > 1 µm in hair
1427 cells lacking Kif1aa (P = 0.71). N = 7 neuromasts for DMSO control and nocodazole for **C** and **F**; n
1428 = 9 and 10 neuromasts for DMSO control and taxol for **D** and **G**; n = 8 neuromasts for control
1429 and *kif1aa* for **E** and **H**. An unpaired t-test was used in **C-H**.
1430
1431
1432
1433
1434

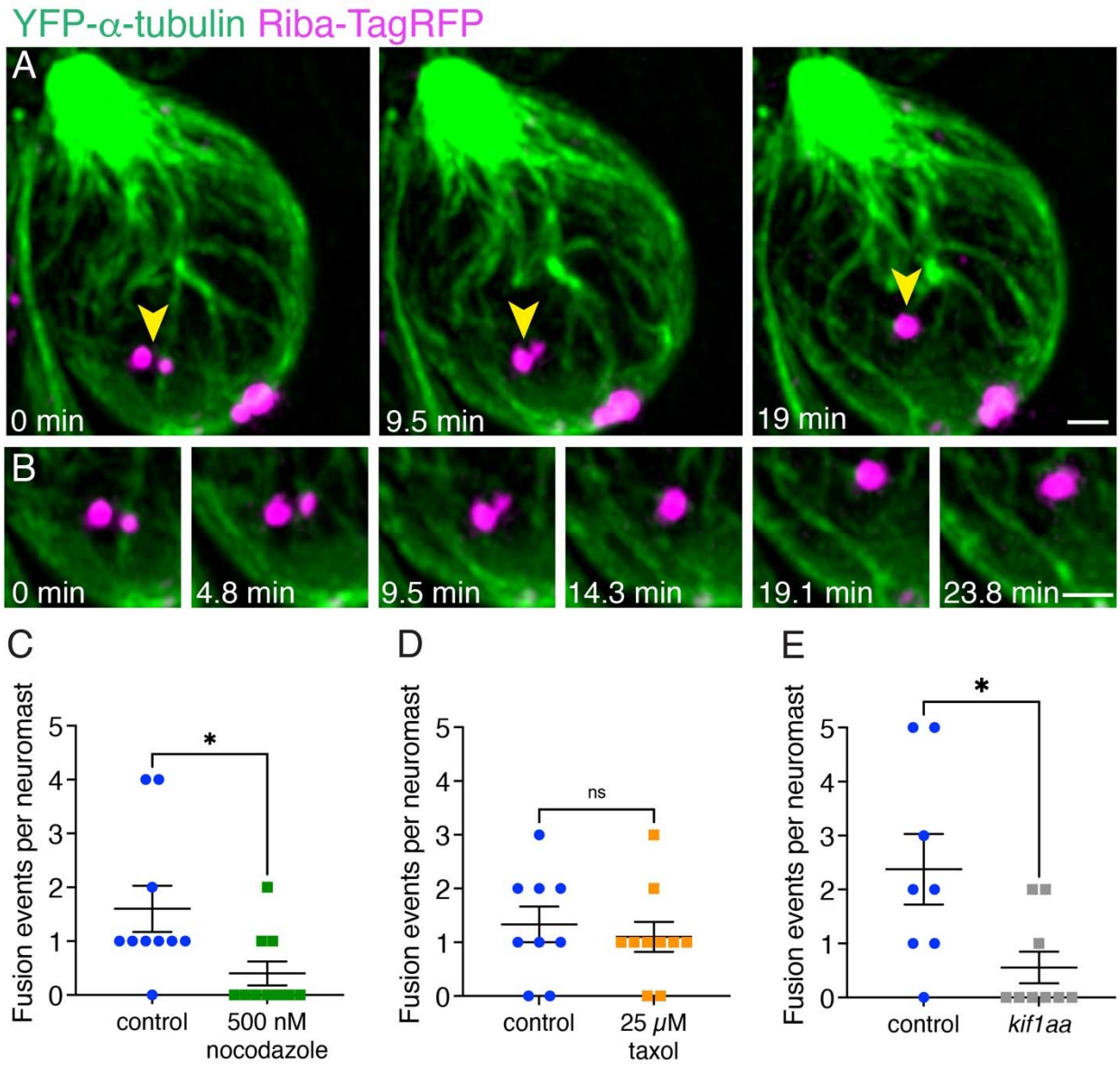

1435

1436 **Figure 8 – Microtubules and Kif1aa are required for fusion events**

1437 **A)** An example of two ribbon precursors undergoing fusion on microtubules (yellow

1438 arrowheads). **B)** A zoomed-in montage of the example from **A** is shown where the association

1439 of each precursor with microtubules can be seen during the process of fusion (also see Movie

1440 S9). **C-D)** Destabilizing the microtubules with nocodazole treatment reduces the number of

1441 fusion events observed in timelapses (P = 0.023). Taxol treatment has no effect (P = 0.60). **E)**

1442 Loss of Kif1aa significantly reduces the number of fusion events observed in timelapses

1443 compared to control (P = 0.018). N = 10 neuromasts for DMSO control and nocodazole for **C**; n =

1444 9 and 10 neuromasts for DMSO control and taxol for **D**; n = 8 and 9 neuromasts for control and
1445 *kif1aa* for **E**. An unpaired t-test was used for comparisons in **C-E**. Scale bars in **A** and **B** = 1 µm.
1446
1447
1448
1449
1450
1451
1452
1453
1454
1455
1456
1457
1458
1459
1460
1461
1462
1463
1464
1465
1466
1467
1468
1469
1470
1471
1472

1473 **Supplemental Figures**

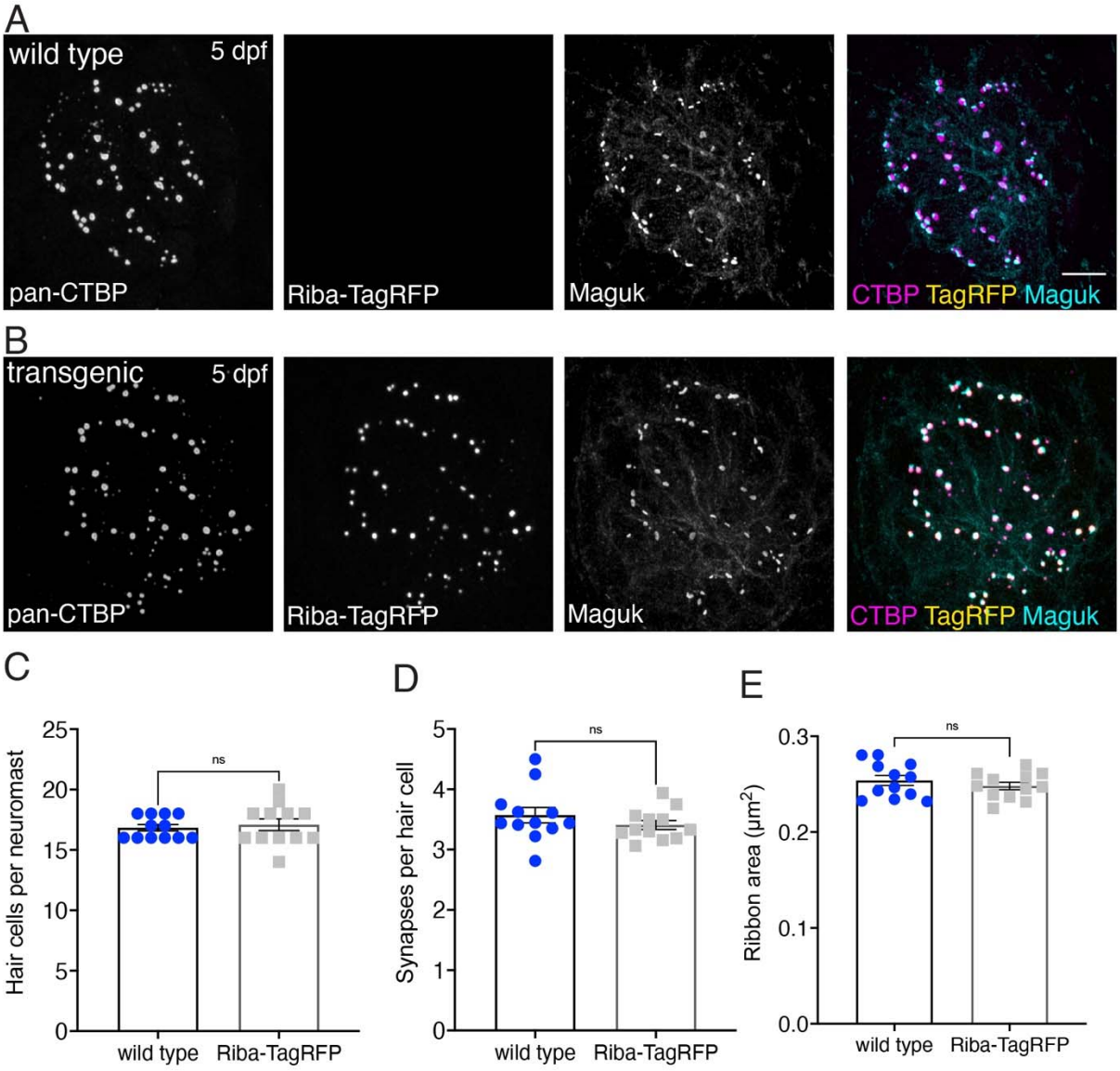

1474

1475 **Figure 1-S1 – Riba-TagRFP transgenic fish have normal cell numbers, synapses per hair cell,**

1476 **and ribbon areas.**

1477 **A-B)** Example immunostained images from pLL hair cells of wild type **(A)** and Riba-TagRFP

1478 transgenic fish **(B)** are shown at 5 dpf. The neuromasts are labeled with pan-CTBP (labels

1479 ribbons) and Maguk (labels postsynapses). **C-E)** Quantification of these images shows no

1480 significant differences in the number of hair cells (**C**, P = 0.728), the number of synapses per hair

1481 cell (**D**, P = 0.283), or the ribbon areas > 0.1 μm^2 (**E**, P = 0.392) between the wild type and

1482 transgenic (n = 12 neuromasts for wild type and Riba-TagRFP). For comparisons a Mann-Whitey
1483 test was used in C and an unpaired t-test was used in **D-E**, scale bar in **A** = 5 µm.
1484
1485
1486
1487
1488
1489
1490
1491
1492
1493
1494
1495
1496
1497
1498
1499
1500
1501
1502
1503
1504
1505
1506
1507
1508

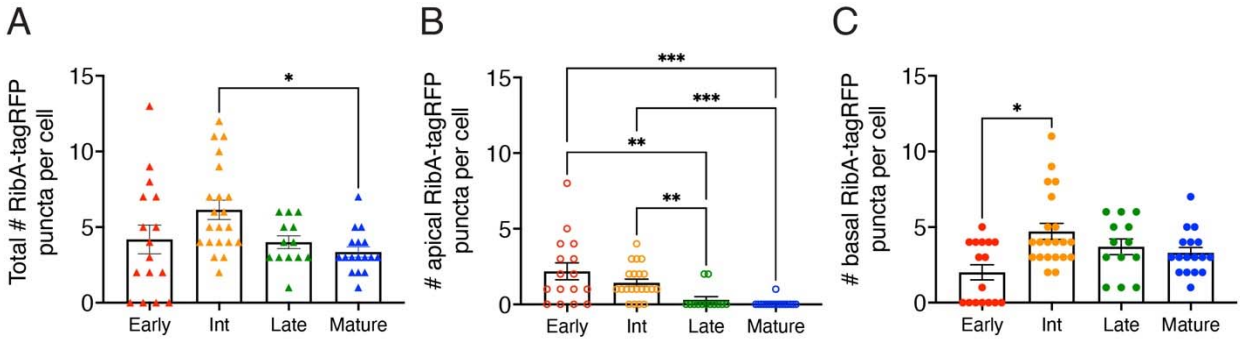

1509
1510 **Figure 1-S2 – Ribbon number and apical-basal localization changes during development**

1511 **A)** The total number of Riba-TagRFP puncta increases from early to intermediate stages. The
1512 total number of puncta becomes significantly reduced upon maturation. **B)** The number of
1513 apically-localized Riba-TagRFP precursors is high at early and intermediate stages and is
1514 significantly reduced compared to late and mature hair cells. **C)** The number of basally-localized
1515 Riba-TagRFP ribbons is low at early stages and becomes significantly higher by intermediate
1516 stages. For comparisons, a Kruskal-Wallis test was used in **A-C**, * $P < 0.05$, ** $P < 0.01$, *** $P <$
1517 0.001.

1518

1519

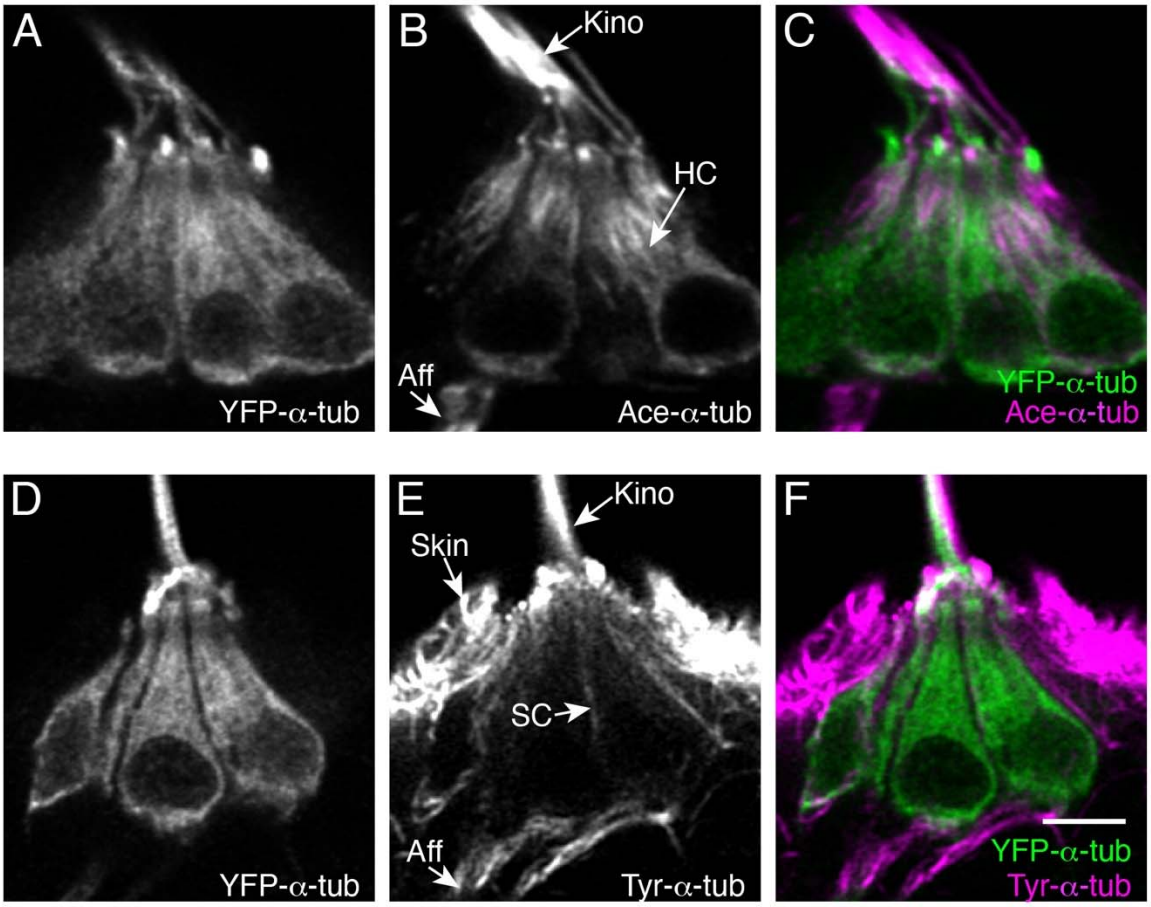

Figure 2-S1 – Microtubule modifications in lateral-line hair cells

A-F) Example immunostains of pLL hair cells expressing YFP-α-tubulin at 5 dpf, labeled either with acetylated-α-tubulin (**A-C**) or tyrosinated-α-tubulin (**D-F**). Panels **A** and **D** show YFP-α-tubulin, **B** and **E** show acetylated-α-tubulin or tyrosinated-α-tubulin labels respectively. Panels **C** and **F** show the merged images. HC = hair cell; SC = supporting cell; Aff = afferent process; Kino = kinocilium; Scale bar in **F** = 5 µm.

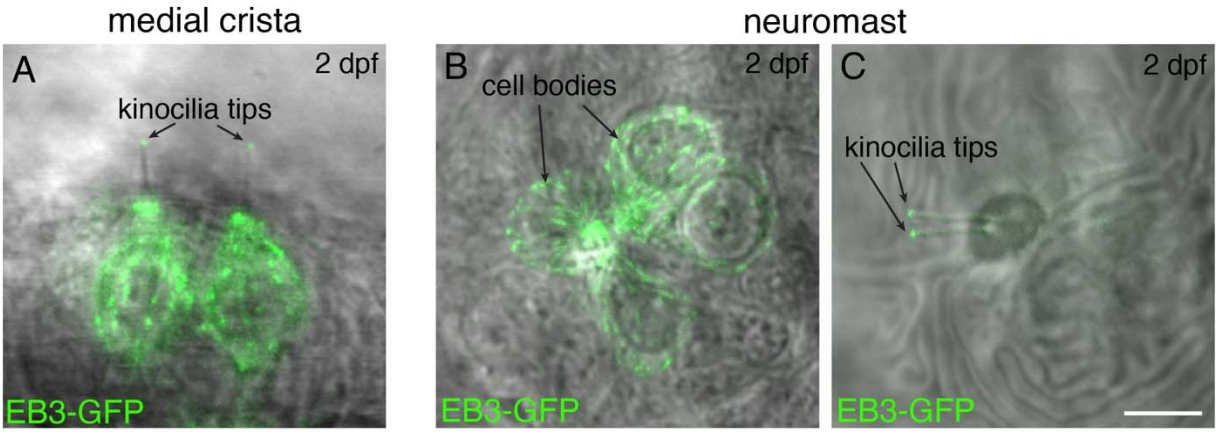

Figure 2-S2 – EB3-GFP label reveals microtubule (+) ends at kinocilial tips in hair cells

A) Example side-view image of EB3-GFP localization in 2 hair cells of the medial cristae within the zebrafish inner ear at 2 dpf. **B-C)** Example images of EB3-GFP localization in 4 hair cells within a pLL neuromast at 2 dpf. In **B**, a maximum-intensity projection of EB3-GFP localization in the cell bodies is shown. In **C**, a more apical projection shows the localization of EB3-GFP in the kinocilia of the same hair cells as **B**. In both zebrafish inner ear and pLL hair cells EB3-GFP is present in the cell bodies and at the tips of kinocilia. In all images EB3-GFP is overlaid onto a transmitted light image. Scale bar in **C** = 5 µm.

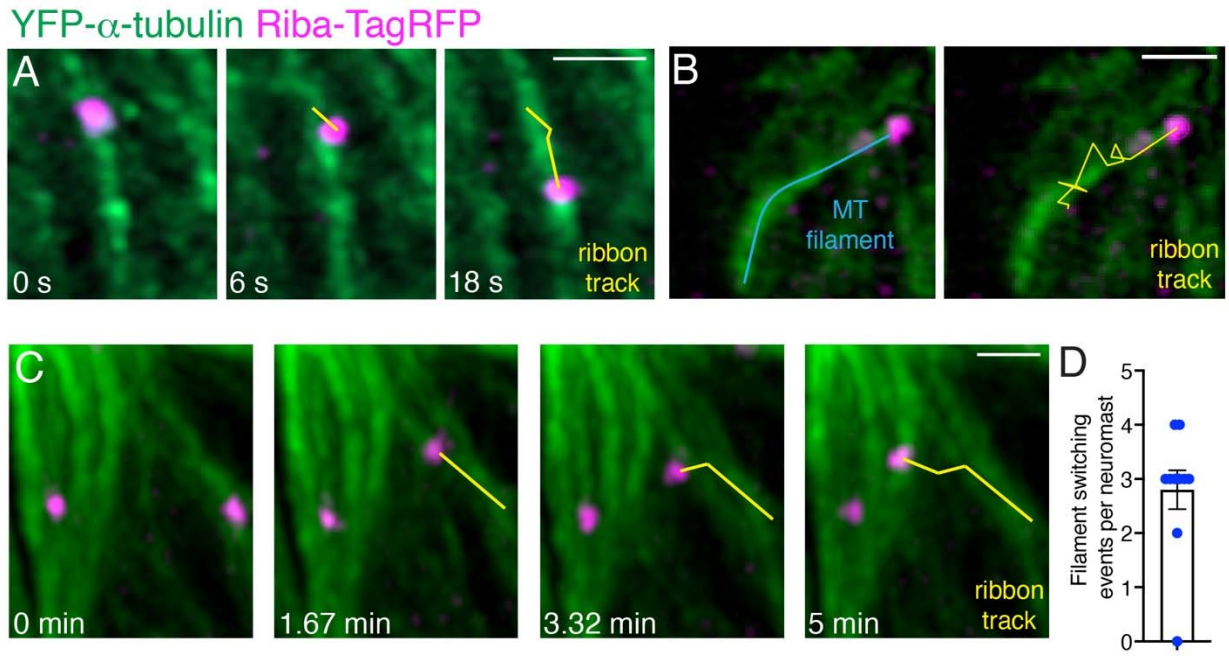

Figure 3-S1 – Ribbons move directionally on microtubules and can move between microtubule filaments

A) Example of ribbon movement on a microtubule directed towards the cell base. Ribbon precursor movement was imaged at 3 s intervals for ~5 min. Shown in **A** are frames 10, 12 and 16 (also see Movie S5). **B)** Example of a ribbon movement along a microtubule towards the cell apex. Images were acquired every 50 s for ~40 min. The microtubule (MT) filament is indicated in blue. The track of the ribbon over frames 25-46 (21 frames, 17.5 min) is shown in yellow. The track is overlaid onto the last image of the timelapse (also see Movie S6). **C)** Example of a ribbon moving along a microtubule towards the cell apex and then switching to another microtubule. Images were acquired every 98 s for 43 min. Shown in **C** are frames 10, 12, 14, and 16 (also see Movie S7). **D)** Quantification shows an average of 2.8 filament switching events per neuromast during timelapses (timelapses acquired every 50-100 s for 30-70 min, n = 10 neuromasts). Scale bars in **A-C** = 1 µm.

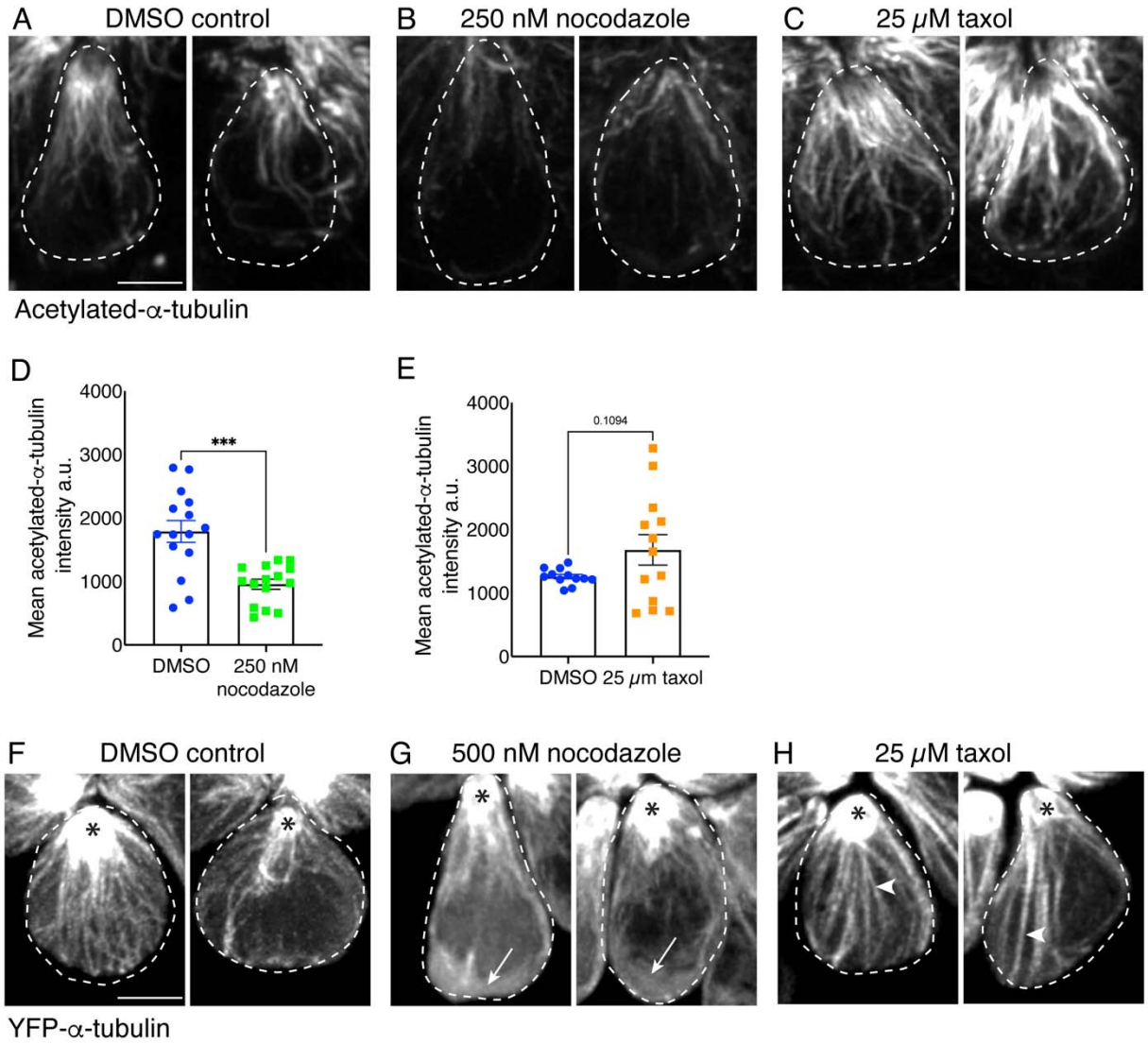

Figure 4-S1 –Nocodazole and taxol treatment impact microtubules in lateral line hair cells

A-C) Example side-view images of individual hair cells treated overnight with 250 nM nocodazole **(B)** or 25 µM taxol **(C)** overnight compared to DMSO control **(A)**. Hair cells were fixed and stained with acetylated-α-tubulin at 3 dpf. In **B**, fewer microtubule networks are observed in nocodazole-treated hair cells. In contrast, in **C**, more intense, stable microtubules are observed in taxol-treated hair cells. **D)** Quantification reveals a significant reduction in the mean acetylated-α-tubulin intensity in hair cells treated overnight with nocodazole, indicating microtubule disruption (n = 15 neuromasts for each condition, P < 0001). **E)** Although the mean acetylated-α-tubulin intensity levels were elevated after treatment with 25 µM taxol overnight, the elevation was not significant (n = 12 neuromasts for DMSO control and 13 for taxol

1568 treatment, P = 0.109). **F-H)** Example side-view images of individual hair cells at 2 dpf expressing
1569 YFP-α-tubulin treated at 2 dpf with 500 nM nocodazole **(G)** or 25 µM taxol **(H)** for 3-4 hrs,
1570 compared to DMSO controls **(F)**. In **G** fewer microtubule networks along with more diffuse YFP-
1571 α-tubulin label (white arrows) is observed in nocodazole-treated hair cells. In contrast, in **H**,
1572 more intense and long, stable microtubules (white arrowheads) are observed in taxol-treated
1573 hair cells. All hair cells in **F-H** show persistent and stable microtubules at the cell apex (black
1574 asterisks). Images in **A-C** and **F-H** were maximum-intensity projected and displayed using the
1575 same settings. For comparisons, an unpaired t-test was used in **D** and **E.** Scale bar in **A** and **F** =
1576 2.5 µm.
1577
1578
1579
1580

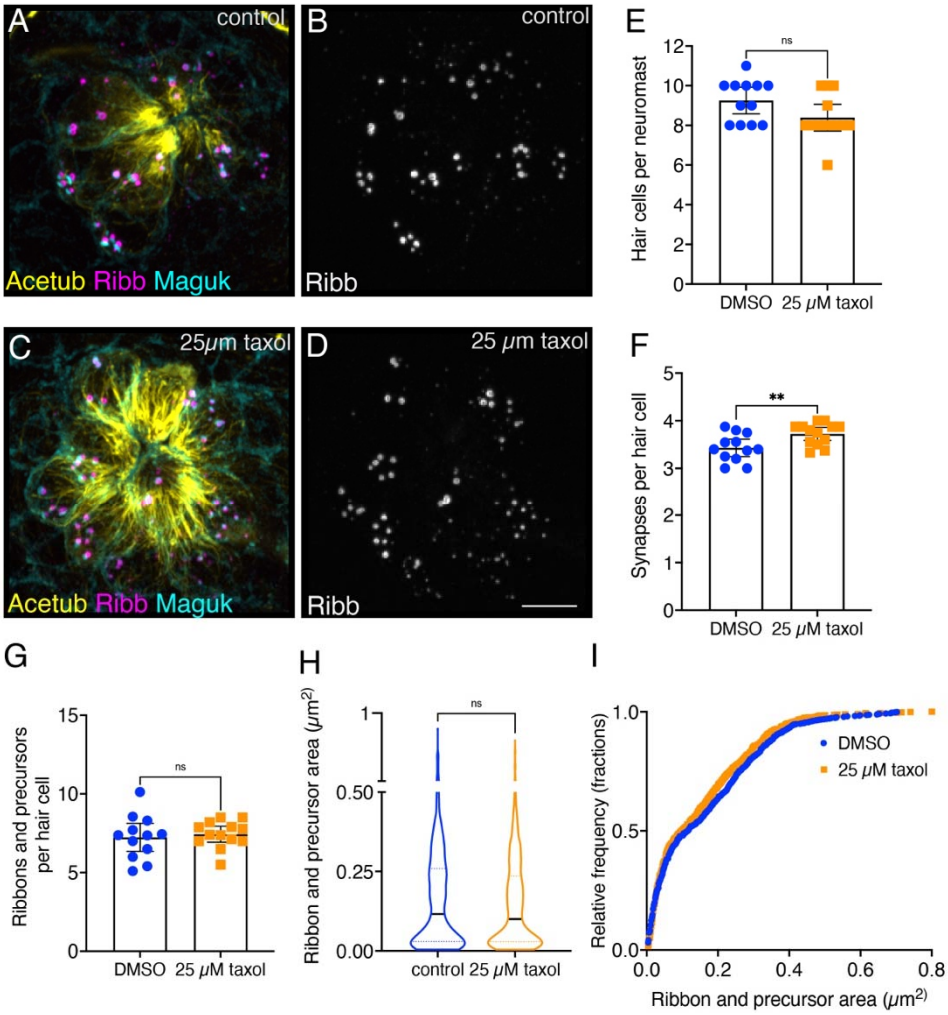

Figure 4-S2 – Overnight microtubule stabilization slightly increases synapse counts

A-D) Example immunostain of a neuromast at 3 dpf after an overnight treatment with 25 µM taxol (**C-D**) or DMSO (**A-B**). Acetylated-α-tubulin (Acetub) labels microtubules, Ribeyeb (Ribb) labels precursors and ribbons, and Maguk labels postsynapses. **E-G**) After an overnight treatment with 25 µM taxol there are similar numbers of hair cells per neuromast (**E**, P = 0.059), more complete synapses per cell (**F**, P = 0.009), and no change in the number of ribbons and precursors per cell (**G**, P = 0.672) compared to controls (n = 12 and 13 neuromasts for control and 25 µM taxol treatments). **H-I**) After an overnight treatment with 25 µM taxol the average area of Ribb puncta was not changed compared to controls (**H**, P = 0.153, n = 800 and 817 Ribb puncta for control and 25 µM taxol treatments). In **I**, the relative frequency of all the areas of Ribb puncta are plotted in taxol treatment and controls. For comparisons an unpaired t-test was used in **E-G**, and a Mann-Whitney test was used in **H**. Scale bar in **D** = 5 µm.

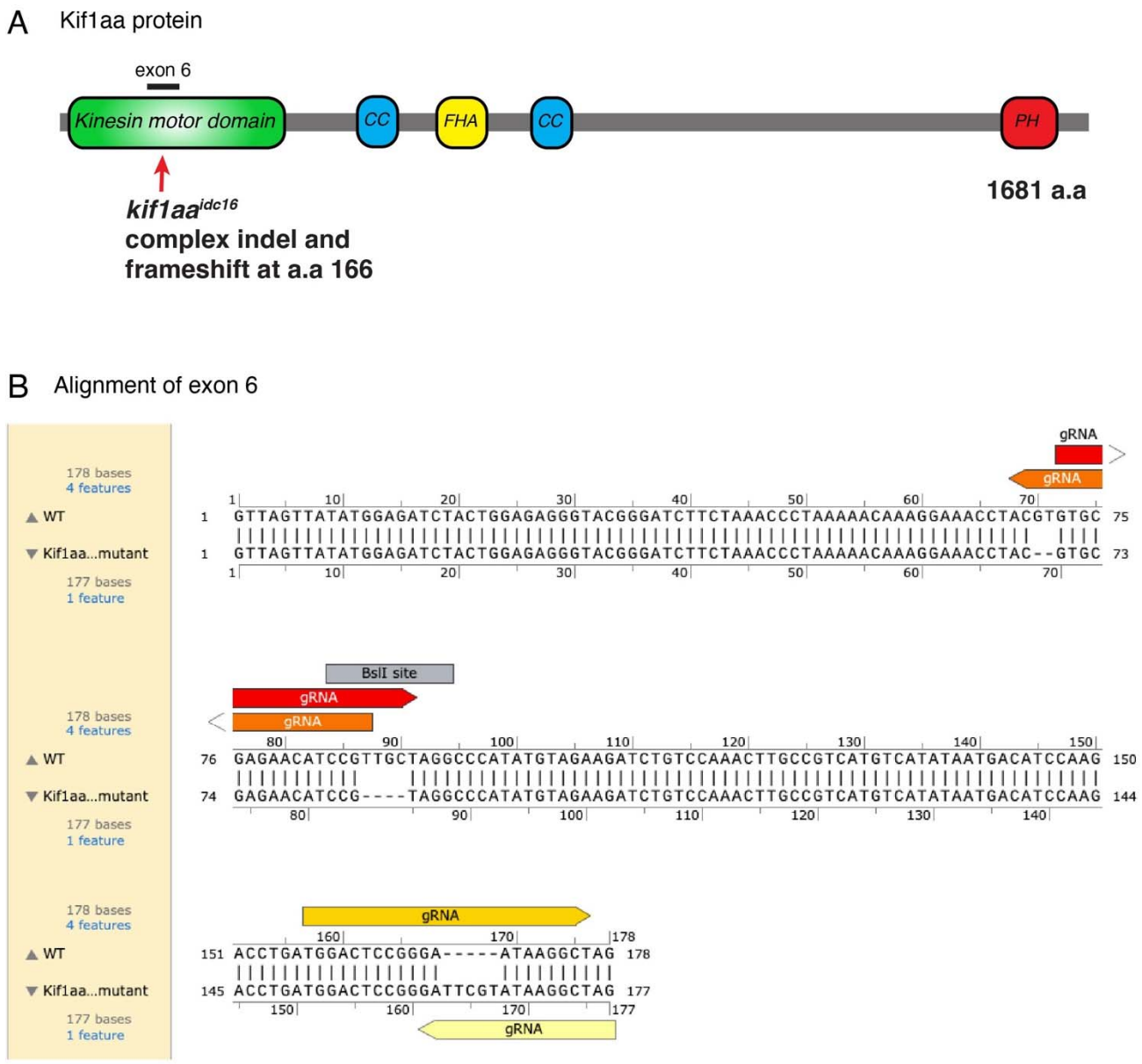

Figure 5-S1 –Kif1aa protein and exon 6 lesions

A) Overview of the Kif1aa protein and major domains (coiled coil (CC), fork-head associated (FHA), pleckstrin homology (PH)). The location of the germline *kif1aa* lesion in the kinesin motor domain within exon 6 is indicated. **B)** The DNA sequence of exon 6 (178 bp) in wild type and *kif1aa* germline mutants. The 4 gRNAs used to make the *kif1aa* germline mutant are shown. 2 deletions and 1 insertion are present in *kif1aa* germline mutants. The BslI restriction site used for genotyping is shown. This DNA alignment was done in Snapgene.

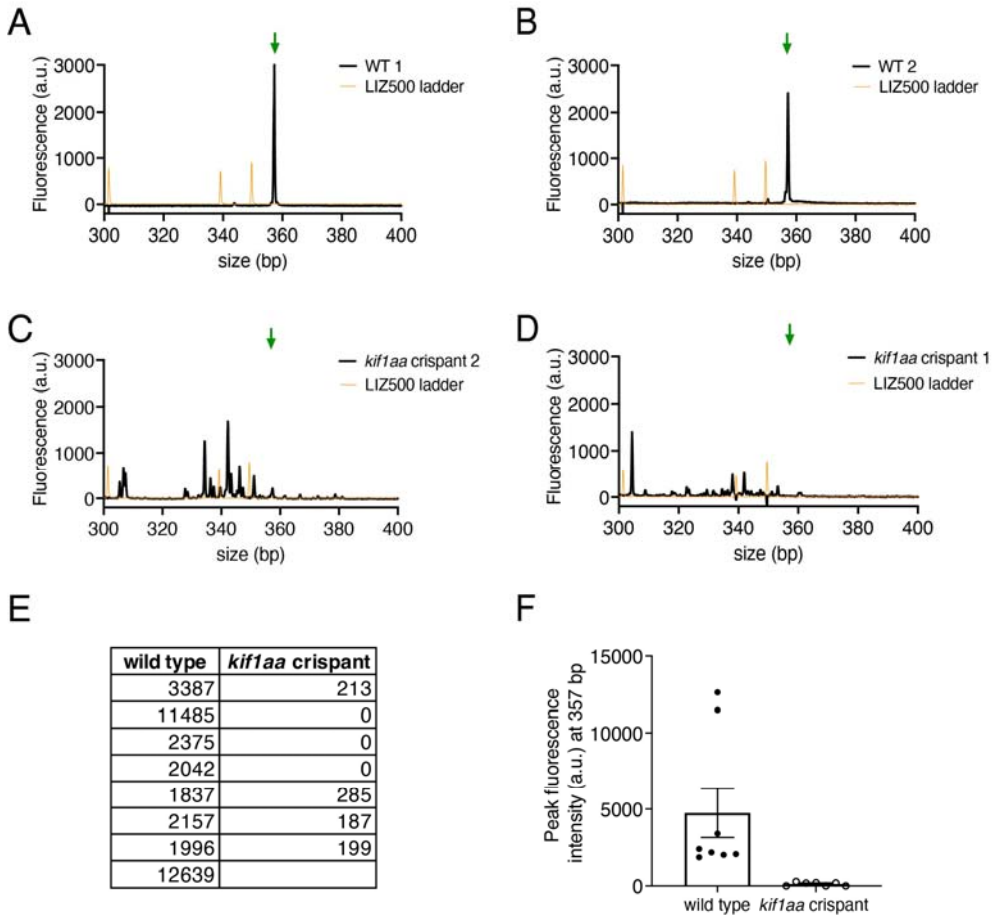

wild type	*kif1aa* crispant
3387	213
11485	0
2375	0
2042	0
1837	285
2157	187
1996	199
12639	

Figure 6-S1 –*kif1aa* crispant verification via genotyping via fluorescent fragment analysis

Each fish that was imaged in our *kif1aa* experiments was genotyped using fragment analysis of fluorescent PCR products (primers: *kif1aa*_FWD_fPCR 5'-TGTAAAACGACGGCCAGT-AAATAGAGATTCACTTTTAATC-3' and *kif1aa*_REV_fPCR 5'- GTGTCTT-CCTAGGCTTACAATGCTTTTGG-3' (Carrington et al., 2015)). **A-D**) Shown are example graphs from wild type (**A,B)** and *kif1aa* crispants **(C,D)**. The wild-type graphs have a distinct peak at 357 bp (green arrow) while the *kif1aa* crispants this peak is dramatically reduced. The multiple secondary peaks in **C-D** are indicative of indels up to ~50 bp in *kif1aa* crispants. **E-F)** Quantification of fluorescence intensity values (a.u.) at 357 bp for wild type and *kif1aa* crispants are shown in a table **(E)** and a graph **(F)**, demonstrating successful genomic cutting in the *kif1aa* crispants. *kif1aa* crispants without robust genomic cutting were excluded from our analyses.

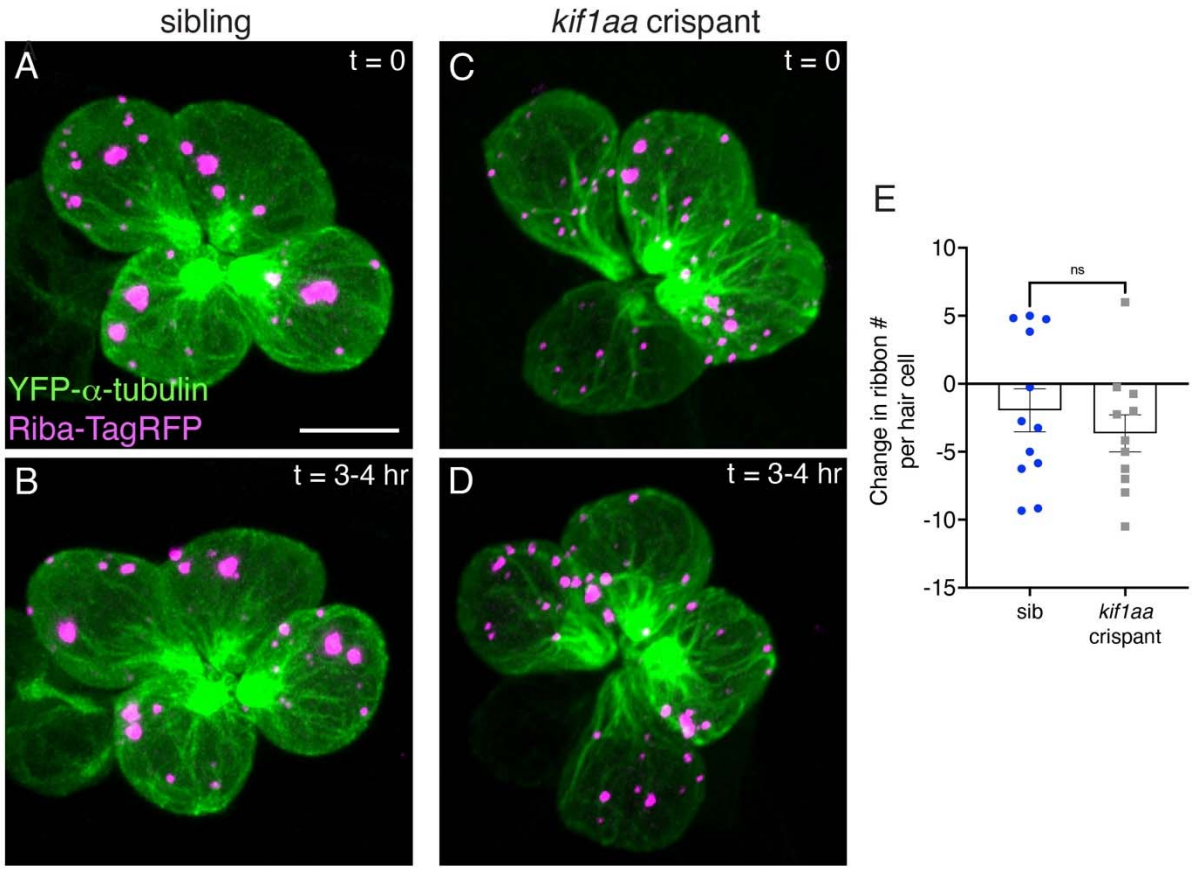

Figure 6-S2 – Loss of Kif1aa does not impact ribbon numbers over 3-4 hrs

A,C) Example images of neuromasts at 2 dpf. The microtubule network and ribbons are marked with YFP-tubulin and Riba-TagRFP respectively. Neuromasts were imaged immediately (**A**, sibling control; **C**, *kif1aa* F0 crispants) and after 3-4 hrs (**B**, sibling control; **D**, *kif1aa* F0 crispants). **E**) Quantification revealed that after 3-4 hrs the number of Riba-TagRFP puncta per hair cell was the same in control and *kif1aa* F0 crispants (n = 12 and 11 neuromasts for control and *kif1aa* F0 crispants, P = 0.427). An unpaired t-test was used for the comparison in **E**. Scale bar in **A** = 5 µm.

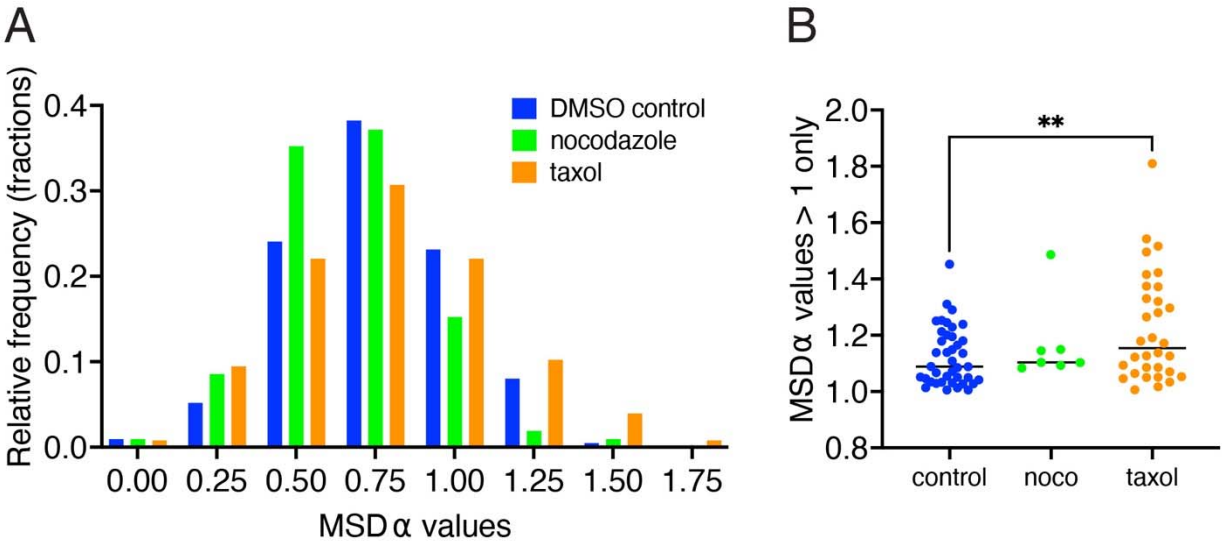

Figure 7-S1 – A more stable microtubule network results in directional ribbon tracks with higher MSD α values

A) Distributions of individual ribbon track MSD α values are shown for control, nocodazole- (500 nM) and taxol- (25 µM) treated hair cells. Compared to control, taxol treatment shifts the distribution towards higher α values, while nocodazole shifts the distribution towards lower α values (total number of tracks analyzed: control (239), nocodazole (113), and taxol (140)). **B)** When examining only α > 1 values (indicative of directional motion), there are significantly higher α values in taxol-treated samples compared to control (P = 0.013). A one-way ANOVA was used for the comparison in **B**.

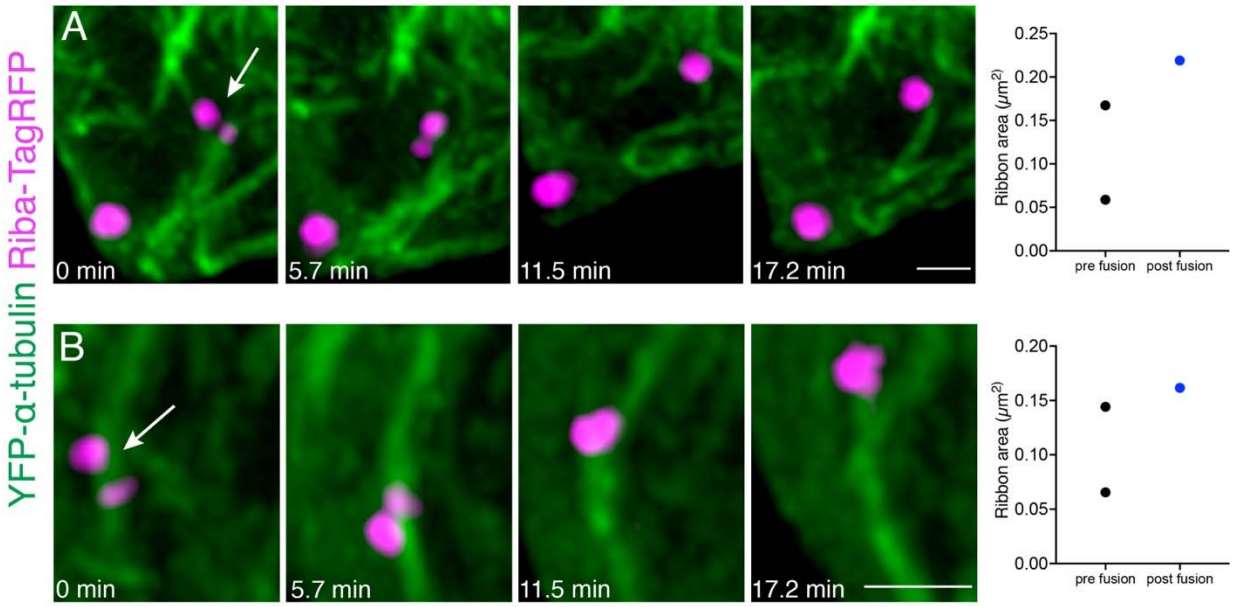

Figure 8-S1 – Ribbon precursor fuse on or near microtubules

A-B) Two examples of ribbon precursor fusion on or near microtubules. Ribbons were tracked over 13 frames that were acquired every 5.7 min. Shown in **A** are frames 3-6. Shown in **B** are frames 4-7. The arrows indicate ribbons of interest. Plotted on the right of each example is the change in area before (pre fusion) the 2 precursors fuse into one larger precursor (post fusion). These examples correspond to Movies S10 and S11. Scale bars in **A-B** = 1 µm.

1667 **Movie Legends**

1668 **Movie S1 – EB3-GFP dynamics in developing lateral-line hair cells**

1669 Timelapse of the example of a pLL neuromast expressing EB3-GFP from Figure 2. The growing or
1670 plus ends of microtubules can be visualized by capturing EB3-GFP dynamics. The timelapse was
1671 acquired on a LSM 780 confocal microscope every 7 s for 22 min. Maximum-intensity projection
1672 of the original z-stack is shown on the left side, played at 5 frames per second. The right side
1673 shows the same movie as the left side except EB3-GFP tracks are color-coded and followed over
1674 time using the FIJI plugin TrackMate. Scale bar = 5 µm

1675

1676 **Movie S2 – Tracking precursors and ribbons in 3D using Imaris**

1677 Timelapse movie of a pLL neuromast at 2 dpf. A partial cell volume was captured at 50 s
1678 intervals for ~30 min with a Zeiss LSM 780 with Airyscan. Microtubules are marked with YFP-
1679 tubulin (green), ribbons and precursors are marked with Riba-TagRFP (magenta). Tracks
1680 captured in Imaris are color coded with time. This example is the same as Figure 3A-B.
1681 Maximum-intensity projections of the original z-stacks are shown, played at 5 frames per
1682 second. Scale bar = 2 µm.

1683

1684 **Movie S3 – Tracking precursors and ribbons in 3D using Imaris**

1685 Timelapse movie of a pLL neuromast at 2 dpf. A partial cell volume was captured at 60 s
1686 intervals for ~30 min with a Zeiss LSM 780 with Airyscan. Microtubules are marked with YFP-
1687 tubulin (green), ribbons and precursors are marked with Riba-TagRFP (magenta). Tracks
1688 captured in Imaris are shown in yellow. Maximum-intensity projections of the original z-stacks
1689 are shown, played at 5 frames per second. Scale bar = 2 µm.

1690

1691 **Movie S4 – Directional motion to cell base and stationary precursors on microtubule**

1692 Timelapse movie of a pLL neuromast at 2 dpf. A partial cell volume was captured at 20 s
1693 intervals for 9 min with a Zeiss LSM 980 with Airyscan 2. Microtubules are marked with YFP-
1694 tubulin (green), ribbons and precursors are marked with Riba-TagRFP (magenta). Maximum-
1695 intensity projections of the original z-stacks are shown played at 5 frames per second. This

1696 example is the same as Figure 3D-E. On the left side is a timelapse of the hair cell showing a
1697 ribbon precursor moving along a microtubule toward the cell base. In addition, a stationary
1698 ribbon precursor is also shown. On the right is a higher magnification view of these two ribbon
1699 precursors. The circles indicate spots identified using TrackMate, along with the track of the
1700 moving ribbon shown in yellow. Scale bar = 2 µm.
1701
1702 **Movie S5 – Directional motion of precursor along a microtubule to the cell base**
1703 Timelapse movie of a pLL neuromast at 2 dpf. A partial cell volume was captured at 3 s intervals
1704 for 5 min with a Zeiss LSM 980 with Airyscan 2. Microtubules are marked with YFP-tubulin
1705 (green), ribbons and precursors are marked with Riba-TagRFP (magenta). Maximum-intensity
1706 projections of the original z-stacks are shown, played at 5 frames per second. On the left side is
1707 a timelapse of the hair cell showing a ribbon precursor moving along a microtubule toward the
1708 cell base. On the right is a higher magnification view of these two ribbon precursors. TrackMate
1709 was used to generate the track of the precursor along the microtubule in yellow. This example
1710 is the same as Figure 3-S1A. Scale bar = 2 µm.
1711
1712 **Movie S6 – Directional motion of precursor along microtubule to cell apex**
1713 Timelapse movie of a pLL neuromast at 2 dpf. A partial cell volume was captured at 50 s
1714 intervals for 18 min with a Zeiss LSM 780 with Airyscan. Microtubules are marked with YFP-
1715 tubulin (green), ribbons and precursors are marked with Riba-TagRFP (magenta). Maximum-
1716 intensity projections of the original z-stacks are shown, played at 5 frames per second. On the
1717 left side is a timelapse of the hair cell showing a ribbon precursor moving along a microtubule
1718 toward the cell apex. On the right is a higher magnification view of this precursor, with the
1719 tracks of the ribbon precursor during the timelapse. The circle indicates a spot identified using
1720 TrackMate, along with the track of the moving ribbon shown in yellow. This example is the
1721 same as Figure 3-S1B. Scale bar = 2 µm.
1722
1723 **Movie S7 – Precursor switching between microtubules**

1724 Timelapse movie of a pLL neuromast at 2 dpf. A partial cell volume was captured at ~100 s
1725 intervals for 40 min with a Zeiss LSM 980 with Airyscan. Microtubules are marked with YFP-
1726 tubulin (green), ribbons and precursors are marked with Riba-TagRFP (magenta). Maximum-
1727 intensity projections of the original z-stacks are shown, played at 5 frames per second. On the
1728 left side is a timelapse of the hair cell showing a ribbon precursor moving along a microtubule
1729 toward the hair cell apex; the precursor then moves to another microtubule. On the right is a
1730 higher magnification view of the ribbon precursor during the timelapse. The precursor
1731 movement is quite fast and at this interval can be observed twice in a single z-stack during
1732 movement between microtubules at timepoints 2,4, and 15. This example is the same as Figure
1733 3-S1C. Scale bar = 2 µm.
1734
1735 **Movie S8 – Microtubule dynamics in hair cells change upon treatment with nocodazole and**
1736 **taxol**
1737 Timelapse movies of pLL neuromasts at 2 dpf captured after treatment with 0.1 % DMSO
1738 (control, left side), 25 µM taxol (Taxol, middle), or 250 nM nocodazole (Noc, right side) for 30
1739 min. Microtubules are marked with YFP-tubulin (gray) and ribbons are marked with Riba-
1740 TagRFP (magenta). The timelapses of partial cell volumes were acquired with a Zeiss LSM 780
1741 with Airyscan every 50-80 s for 30 min. Maximum-intensity projections of the original z-stacks
1742 are shown, played at 5 frames per second. The taxol-treated neuromast has more stabilized
1743 microtubules and very little cytoplasmic tubulin (depolymerized tubulin), indicating that the
1744 microtubules are more stable than the control. In the nocodazole-treated neuromast, there are
1745 fewer microtubules and more diffuse cytoplasmic tubulin compared to the control. Scale bar =
1746 2 µm.
1747
1748 **Movie S9 – Ribbon precursors attached to microtubules undergo fusion**
1749 Timelapse movie of a pLL neuromast at 2 dpf. A partial cell volume was captured at 4.8 min
1750 intervals for 100 min with a Zeiss LSM 780 with Airyscan. Microtubules are marked with YFP-
1751 tubulin (green) and ribbons are marked with Riba-TagRFP (magenta). Maximum-intensity
1752 projections of the original z-stacks are shown, played at 5 frames per second. Two ribbon

1753 precursors associate with microtubules and fuse near the hair cell base. This example is the
1754 same as Figure 8A-B. Scale bar = 2 µm.
1755
1756 **Movie S10 – Ribbon precursors attached to microtubules undergo fusion**
1757 Timelapse movie of a pLL neuromast at 2 dpf. A partial cell volume was captured at 5.7 min
1758 intervals for 75 min with a Zeiss LSM 780 with Airyscan. Microtubules are marked with YFP-
1759 tubulin (green) and ribbons are marked with Riba-TagRFP (magenta). Maximum-intensity
1760 projections of the original z-stacks are shown, played at 2 frames per second. This example is
1761 the same as Figure 8-S1A. Scale bar = 2 µm.
1762
1763 **Movie 11 – Ribbon precursors attached to microtubules undergo fusion**
1764 Timelapse movie of a pLL neuromast at 2 dpf. A partial cell volume was captured at 5.7 min
1765 intervals for 75 min with a Zeiss LSM 780 with Airyscan. Microtubules are marked with YFP-
1766 tubulin (green) and ribbons are marked with Riba-TagRFP (magenta). Maximum-intensity
1767 projections of the original z-stacks are shown, played at 2 frames per second. This example is
1768 the same as Figure 8-S1B. Scale bar = 2 µm.
1769
1770
1771
1772
1773